Politecnico di Torino

Nanotechnologies for ICTs

Master's Thesis Project

HOLLOW MEMS

FABRICATION, FEM SIMULATION AND CHARACTERIZATION OF AN INTEGRATED SENSOR

Supervisor:
Prof. Carlo Ricciardi

Candidate:
Simone Galati
S244099

Supervisors at Technical University of Denmark:
PostDoc Peter Emil Larsen

July 2019

Ex nihilo nihil fit.
De Rerum Natura, Lucrezio

ACKNOWLEDGEMENTS

At the end of my academic route, I would like to thank every person that took part of it, allowing me to become who I am now.

Firstly, thank to my supervisor in Italy - Professor Carlo Ricciardi - who gave me the possibility to enter in such an innovative and interesting scientific field, being always kind and helpful to me.
Many thanks also, and above all, to professor Anja Boisen who offered me the opportunity to work into "Nanoprobes" group, allowing to meet a highly professional reality full of both scientific and human resources. I would like to spend few words for this group and all the other people met at DTU. A special thank goes to Peter, my guide during the period at DTU, for all the precious explanations and for the possibility to pretend to be a real researcher. Then, thanks to Francesca and Laura for the academic and psycholoical support given to me: thanks for every smile, suggestion, coffee and talk, specially during the hardest moments. Also thanks to Chiara, Stine, Morten, V, Sriram, Lasse and Arianna for having been present during this period. I never imagined meeting so many nice people.

Still staying in Denmark, thanks, with all my heart, to my "adventure mates", Saverio, Giorgio, Quentin and Andrea for every moment spent together and mostly for having made, against all expectations, the cold Copenhagen a warmer place full of beautiful memories: i will never forget the taste of "pizza" from Netto.

Now it is the moment to move towards my second home, Torino, that I want to thank since, in almost 6 years, allowed me to meet some of the most important friends of my life. Thanks first to Alberto for the countless and unforgettable music and chass sessions during the 'hard' studying days, and together with Federica, Gabri, Massi, Nicola and Nicolò for being my shoulder since the second year. Thanks for having choosen us one each other and for having shared the most important moments of the last years, I can't imagine how I would have faced these years without the presence of each of them.
Then, thanks to 'Casa Marchisio & Co', Alessandra, Elisa, Eva, Marta, Alessio and Baso, for being there in each moment, for having rejoiced, studied, drunk and laughed together, for being a real family (with the coolest student apartment of the whole town) and for having built the most 'FRIENDS-like' situation one could imagine.
My gratitude goes also to my class mates, Lucrezia, Giuseppe and Maria Chiara, whose presence has been fundamental to evercome all

the boring classes and works, often gladdened by delicious and heavy food.
Many thanks to Maria Teresa, for being a constant presence since the first moment in Torino and without which I would have been lost, thanks to Coniglio for making funny every moment, also the most discouraging ones, and thanks to Marta too, for sharing her comforting and fresh brilliance with me.

Finally, I go down to my home land, where everything started. Thank you, my dear Calabria, for being my favourite place in the entire world, where I always want to come back to and where each time I can find all that I need. Thanks for reminindig me that the best things of my life are the simplest ones and that for enjoying everything life offers me I must always keep in mind from where and thanks to who I left. From there, I would like to mention who during these years shared all my important moments despite the distance. Thus, thanks to Alba, Ines, Michele, Ilaria, Piergiu and Giulia, my six horcrux, pieces of my soul, from which actually I was never so far as it has physically been.

The last but not least thanks goes to my family, whose support is always essential in each step I make. Thanks to my dad, for always believing in me and for having trained my brain since I was born with his strange way to talk. Thanks to my shiny mum, who taught me to smile, always, in front of each kind of senseless situation life can deliver you. Thanks to my grandma Pina for always showing pride and extreme sweetness to me.
To conclude, the biggest thanks is addressed to my big brother, Dario, my opposite in everything, but anyway, the person who teaches me the most how important it is that whatever you decide to do in your life, you have to do it with passion.

RINGRAZIAMENTI

Alla fine del mio percorso universitario, vorrei ringraziare ogni persona che ne ha preso parte, permettendomi di diventare ciò che sono ora.

Per iniziare, grazie al mio relatore in Italia - il Professore Carlo Ricciardi - per avermi introdotto in un campo scientifico tanto innovativo e interessante e per essere sempre stato gentile e disponibile nei miei confronti.
Molte grazie inoltre, e soprattutto, alla Professoressa Anja Boisen, che mi ha offerto la possibilità di lavorare nel gruppo "Nanoprobes", permettendomi di venire a contatto con una realtà estremamente professionale e piena di risorse, umane e scientifiche. A tal proposito, vorrei spendere alcune parole per il gruppo e per tutte le altre persone che ho conosciuto in DTU. Un grazie speciale va a Peter, la mia guida durante la mia permanenza in Danimarca, per tutti i preziosi insegnamenti e per avermi dato la possibilità di far finta di essere un vero ricercatore. Poi, grazie a Laura, Francesca, Chiara, Stine, Morten, V, Sririam, Lasse e Arianna per il supporto accademico e psicologico: grazie per ogni sorriso, suggerimento, caffé e chiacchierata, soprattutto nei momenti più duri. Non avrei mai immaginato di incontrare così tante persone gentili.

Rimanendo in Danimarca, grazie con tutto il cuore ai miei compagni di avventura, Saverio, Giorgio, Quentin e Andrea per ogni momento passato insieme e soprattutto per aver reso, contro ogni aspettativa, la fredda Copenaghen un posto caldo e pieno di bellissimi ricordi: non dimenticherò mai il gusto della "pizza" di Netto.

Ora è il momento di spostarsi verso la mia seconda casa, Torino, che voglio ringraziare perché, in quasi sei anni, mi ha permesso di incontrare alcuni dei più importanti amici della mia vita. Grazie ad Alberto per le innumerevoli e indimenticabili sessioni di musica e scacchi durante i giorni di 'duro' studio, e insieme a Federica, Gabri, Massi, Nicola e Nicolò, per essere stati al mio fianco fin dal secondo anno. Grazie per esserci scelti l'un l'altro e per aver condiviso i più importanti momenti degli ultimi anni, non posso neanche immaginare come avrei potuto affrontarli senza la presenza di ognuno di loro.
Grazie inoltre a "Casa Marchisio & Co", Alessandra, Elisa, Eva, Marta, Alessio e Baso, per esserci stati in qualsiasi momento, per aver gioito, studiato, bevuto e riso insieme, per essere stati una bellissima famiglia (con la casa più figa che potesse capitare).

Ringrazio anche i miei compagni di corso, Lucrezia, Giuseppe e Maria Chiara, la cui presenza è stata fondamentale per superare tutte le noiosissime lezioni e progetti, spesso allietati da buono e ben condito cibo.
Molte grazie a Maria Teresa, per essere stata una presenza costante fin dal primo momento a Torino e senza la quale sarei stato sicurmente perso, grazie alla Coniglio per rendere divertente qualisiasi situazione, anche la più scoraggiante e grazie anche a Marta, per aver condiviso con me la sua confortante e fresca brillantezza.

Infine, voglio scendere verso la mia terra, dove tutto è iniziato. Grazie, mia cara Calabria, per essere il mio posto preferito nel mondo, dove voglio sempre tornare e dove riesco sempre a trovare ciò di cui più ho bisogno. Grazie per ricordarmi che le cose più belle della mia vita sono le più semplici e che per godere di tutto ciò che la vita mi offre bisogna sempre tenere a mente da dove e grazie a chi sono partito. Da lì, vorrei menzionare chi durante questi anni ha condiviso tutti i miei momenti importanti nonostante la distanza. Perciò, grazie Alba, Ines, Michele, Ilaria, Piergiu e Giulia, i miei sei horcrux, pezzi della mia anima, da cui in realtà non mi sono mai sentito così lontano come lo sono fisicamente stato.

Gli ultimi, non per importanza, ringraziamenti vanno alla mia famiglia, il cui supporto è sempre essenziale in ogni singolo passo. Grazie a mio padre, per credere sempre in me e per aver allenato il mio cervello fin da appena nato col suo strano modo di parlare. Grazie alla mia luminosa madre, per insegnarmi a sorridere, sempre, di fronte a qualsiasi tipo di assurda situazione che la vita possa presentarti. Grazie a mia nonna Pina per mostrare orgoglio ed estrema dolcezza nei miei confronti, a prescindere. E per concludere, il più grande grazie va a mio fratello, Dario, il mio opposto in qualsiasi cosa, ma comuque la persona che più mi insegna quanto sia importante che qualsiasi cosa tu decida di fare nella vita debba essere fatta con passione.

ABSTRACT

This work describes the Master's Thesis project carried out at the Technical University of Denmark. The goal of the project is to design, fabricate, simulate and characterize a hollow MEMS sensor able to detect individual circulating immuno cells, to study their mechanical properties and also to investigate their response during a specific treatment. Combined density, viscosity, mass spectroscopy and IR absorption spectroscopy can be performed by tracking changes in the sensor's resonant behavior.

Based on a previous work, the design is optimized in order to face the requirements of the current cells shape and dimension leading to the development of a detailed microfabrication process.
Before implementing the process flow, a finite element method (FEM) analysis of the system is performed, with the goal of verifying that the chosen design would be able to measure the intended effects, thus predicting the resonant behaviour of the system. In particular, the resonant frequency is monitored during the flow of a cell through the structure in order to ensure a detactable resonance shift. The simulations are performed in different conditions showing an acceptable shift of the frequency of ~ 1000 ppm when the cell moves from the beginning of the channel to the central point. Specifically, assuming a noise level below 100 ppm, an acceptable approximeted signal to noise ratio (SNR) > 10 is obtained.
At the end of the work, the fabricated structure is characterized in its resonance frequency perfromances. The first flexural mode is measured together with the Quality factor through the vibrometer, resulting in Quality factor values $> 10^3$. In order to verify a sufficient frequency stability, Allan Deviation measurements are performed by emplying a Phase-Locked Loop (PLL) control system to track the resonance frequency over time, confirming the theoretical behaviour of the curve and verifying that sensitivity is mainly limited by white noise at short integration times and frequency shift (random walk) towards longer integration times, with a minimum Allan Deviation of the order of ~ 1 ppm at variable integration time depending on the implemented strucure, ranging from few seconds to some fraction of seconds to tens of seconds.

CONTENTS

LIST OF FIGURES

LIST OF TABLES

ACRONYMS

AD Allan Deviation

AOE Advanced Oxide Etching

BHF Buffered Hydrofluoric Acid

DRIE Deep Riactive Ion Ething

DUV Deep Ultra Violet

FEM Finite Element Method

IR InfraRed

LDV Laser Doppler Vibrometer

LOD Limit Of Detection

LPCVD Low Pressure Chemical Vapour Deposition

MEMS Micro Electro-Mechanical Systems

MSA Micro System Analyser

MSV Microscope Scanning Vibrometer

OM Optical Microscopy

PECVD Plasma Enhanced Chemical Vapour Deposition

PI Proportional Integral

PLL Phase Locked Loop

PMA Planar Motion Analyser

SCR Surface Channel Resonator

SEM Scanning Electron Microscopy

SMR Suspended Micro Channel Resonator

SNR Signal to Noise Ratio

SON Silicon-On-Nothing

SRN Silicon rich Silicon Nitride

Part I

INTRODUCTION AND THEORETICAL BACKGROUND

1 INTRODUCTION

The advances in micro fabrication during the past decades has led to a continous miniaturization of devices allowing the development of micro and nano-electro-mechanical systems (MEMS and NEMS) able to detect physical quantities such as molecular mass, biochemical reactions, quantum state, coupled resonance and so on. The great advantage of micro and nano sized mechanical structures is that their performances increases by lowering their dimensions: the resonant frequency is indeed proportianal to $\propto L^{-2}$ leading to an increase of the frequency and thus also of the device sensitivity up to the eventual detection limit of a single atom [1]. For that reason, this kind of devices are showing a more and more significant interest from the scientific community due to their wide range of application, expecially in the nano-medicine field for the characterization of songle molecules properties and behaviour.

1.1 MOTIVATION AND SCOPE

One of the emerging and at the same time challenging frontiers of fundamental biological research is concerned with the investigation of the mechanical properties of cells at the micro and nano scale.
Among the several innovative applications of this kind of sensors, the most interesting results are carried out for the monitoring of the cells growth during their life cycle, the investigation of the evolution of bacteria colonies and also the analysis of the changes in their mechanical properties of cancer cells.
The cell growth includes variations in both its mass and volume, whose changing is strictly related to the cell cycle. Thus, in order to understand the cell cycle and to identify the cell type and state, a way to measure the mass, volume and density of cells is required. In particular, cells need to coordinate the growth and division during their exponential growth in order to maintain the distribution of the population's size. Even if it is not well defined how cells are able to monitor and regulate cell cycle entry in response to cell sizes, it is known that in the cell cycle control a key rule is given by the concentration of critical regualtory proteins of the cell. This concentration depends on both expression levels and volume of the cell, so that changes the rate of mass and volume accumulation can be correlated to the cell cycle position and can be measured from the cell density variation .
Several methods for monitoring the cell density exploit indirect mea-

surements and density gradients, that can lead to conflicting results due to for example excessive sample manipulation or possible interaction between the cells and the gradient medium.
For this reason the ideal measurement would directly track mass and volume of a cell within a population, minimizing the perturbation due to the sample and allowing to get subsequent measurements.
A smart solution to face this goal is to use suspended microchannel resonators (SMR) able to precisely measure single-cell bouyant mass [2] [3]. This kind of system is a silicon-based cantilever embedded with a microfluidic channel in which individual cell flow inside a medium. The channel resonates is characeterized by a certain resonance frequency proportional to its total mass that varies with the presence of the cells inside.
This results an important techinque since it provides mass and volume information measuring cells in a very wide range of medium withouth requiring any density gradient chemical.
Another important application regards the detection of bacteria. The use of mechanical resonator allows to immobilize molecular receptros (antibodies or DNA molecules) on their surface in order to enable molecular recognition between the target molecules present in a sample solution and the sensor-anchored receptors giving rise to a change of the opetical, electrical or mechanical properties depending on the class of sensor used, without requiring previous labelling. The use of mechanical resonators thus, optimize the time consuption since does not need a prepation of the entities and also avoids a background noise signal due to the possible interference that labels could have with the molecular recognition. Furthermore, another fundamental advantage is the inherent small sensing area allowing analysis of very small sample amounts [4]. In particular, the absorption of bacteria on a resonant cantilever can produce either negative or positive shift in the resonance frequency depending both on the position and extent of the bacteria on the resonator with respect to the shape of the vibration mode used in the measurement. Through this kind of analysis it is possible to understand if this behaviour is due to the stiffness of the cells that increases the flexural rigidity of the cantilever or the added mass effect.
The use of these kind of resonators shows an important rule also in the characterization of the deformability and of the surface frinction of cancer cells [5]. The quantification of the changes of cells during metastatic process remains indeed an important challenge for the understanfig of the mechanism of development and for identifying new therapeutic targets. In particular, the biomechanics of cancer cells has a main rule during metastasis due to the fact that they can travel through small capollaries in order to reach long distances. Thus, cells motion results to be influenced by the viscoelastic and frictional properties as well as by the forces present between the cell and the chan-

nel wall. In the end, besides measuring the cell size as previously explained, in this case also the velocity of the cell entering the microchannel and the transit velocity inside it can be measured, giving so information about also the cell deformability and the friction with the wall.

1.2 STATE OF THE ART

Among the world, several research groups are working on these suspended microchannel resonator sensors, due to the fact that can be differently designed depending on the specific aim they are conceived. Furthermore, they are very versitile sensors, also from an application point of view overcoming the conventional sensing methods. An example is the use of microcantilevers used for the quantitative detection of multiple proteins through specific biomolecular binding leading to diagnostic prostate cancer [6].
Also, a wide range of shape, ideally without any limitation, can be implemented to mechanically trap and continually monitor single cells in order to measure changes in their size and growth in response to specific stimuli [7].
Furthermore, recent studies are developed in order to improve the fabrication process of these devices, that results costly and rather challenging. Both optimization of standards microfabrication processes [8] and implementation of new techniques such as the SON process [9] are currenty being developed in order to have greater degree of freedom in the design of the micro-channel allowing also to further scale the device dimensions keeping reasonable the performances of the resonator behaviour. Other studies are carried on the 3D fabrication through laser direct writing approach able to define the suspended resonant structure and the microfluidic channel in only one step [10]. Thanks to this, fused silica substrates can be used guaranting a totally transparent resonator and thus allowing the coupling of optical and mechanical analysis.

1.3 FABRICATION PROCESS SELECTION

The scope of this work is to develop a versatile hollow MEMS sensor capable of a wide range of measurements, thus able to work with different kind of biosamples immersed in different types of solutions (biofluids, chemicals, buffer solutions, etc.). In order to chose the ideal processes, the following requiremets are taken into account:

- Mass/density sensitivity for single cells mass spectroscopy

- channel diameter varying in order to be large enough to allow the immuno cell transit until the center of channel where it becomes smaller than the average cell diameter (14.1µm)
- IR absorption spectroscopy requirements:
  - high temperature sensor responsivity
  - IR transparency of resonator materia
  - electrical actuation and read out can be necessary to make room for the IR source in order to measure the absorption vs wavelength profile
- highly precise tunability of the microfluidics flowrates

Due to the fact that the channel has to fit the size of the cells, the sacrificial layer based processes are not taken into account.

Furthermore, the IR absorption spectroscopy requires a resonator material transparent to the IR source. This is in combination with the weight requirement coming out from a theoretical point of view asserting that the maximum resonator mass is of the order of 100µg in order to get a mass sensitivity of about 1 pg allowing a relative shift of the resonance frequency proportional to the mass change of the oscillating system. These requiremets lead to eliminate the commercially available micro capillares.
Moreover, in order to measure the heating effects of the absorbed IR radiation, a high heating resposivity is demanded. This results to be based in some MEMS devices on thermal expansion leading to changes in resideual stress of the resonator material [11] [12]. The fabricaiton processes based on the bonding of two micro machined wafers is also excluded because of the lack of residual stress in the resonator.

This leads to exploit the surface channel approach, that can be adapted to all the previously described requirements and for this reason the resonant MEMS sensor structures are referred as surface channel resonator (SCRs).
The resonator material SRN shows very useful properties, even if their exact value depends on the thickness, stress, deposition recipe, temperature, etc.:

- high Young modulus, of the order of hundreds of GPa
- moderate mass density
- high thermal expansion coefficient
- high heating responsivity thanks to the residual stress leaded to the LPCVD SRN deposition [13]

- transparency to IR light

Several advantages can be exploited by means of this kind of approach, leading to a very versatile sensor:

- the size of the channel can be easily adjusted by changing the dry etching parameters
- the mass of the resonator can be minimized by lowering the dimensions of the initial slit in the dielectric
- the use of silicon wafer for the realization of the channel makes it possible to obtain a perfectly smooth SRN surface.

1.4 CHAPTER SUMMARY

- **Chapter 2**: the theoretical background is presented in order to give the mathematical basis for the understanding of the physical behaviour of a micromechanical resonator;
- **Chapter 3**: the main microfabrication and characterization techniques with the relative equipment exploited for the SRN fabrication are introduced from a theoretical point of view. Then, all the steps are sequentially described;
- **Chapter 4**: COMSOL Mupltiphysics software is used to simulate the resinance behaviour of the structure in presence of a single cell travelling through it.
- **Chapter 5**: the equipment setup implemented for the measurements is firstly described. Afterwards, the outline of the experiment procedure is shown.
- **Chapter 6**: the chapter is divided in two main sections, the first regarding the optimization results obtained during the fabrication steps in order to build the SMR facing the design requirements. Then, the results obtained from the frequency characterization of the fabricated structures are carried out.
- **Chapter 7**: general conclusions and future prospectives and improvements are discussed in this chapter, showing the great application prospective that such a resonating sensors can have in the health technology and nanomedicine fields.

2 THEORY

This chapter has the aim to provide the theoretical framework necessary to understand the behaviour of a continuum nanomechanical resonator describing the physical laws that rule the behaviour of a pre-stressed resonator. In particular, the experiments of this work are based on the monitoring of the shift of the resonance frequency of the resonator in order to measure a property of the sample, i.e. mass, density, etc.

2.1 RESONANCE FREQUENCY

In an ideal lossless mechanical structure, the kinetic energy related to a specific mechanical vibration is equal to the potential energy stored in the respective vibrational deformation (equipartition theorem). Continuum structures are characterized by several vibrational eigenmodes at which this situation occurs. At the eigenfrequency, there is a continuus passage from kinetic to potential energy; so when energy is provided to the structure, the system starts oscillating at that precise eigenfrequency with a constant vibrational amplitude.
Dealing with real systems, not the entire energy is converted from kinetic to potential and vice versa due to energy lost in every vibration cycle. This energy dissipation leads to the real resonator to oscillate only for a finite amount of time until the energy is lost. In such a real mechanical structure, the eigenmode mechanism is called *resonance* and the relative frequency at which there is the commutation between kinetic and potential energy is called *resonance frequency*. Since the resonance frequency results to be close to the eigenfrequency of the same system assumed ideal, it is estimated starting from the relative eigenfrequency calculated through analitical models or FEM simulations.
To obtain a further accurate evaluation of the individual eigenmode, an equivalent lamped-element model is exploited in order also to include dissipations [14].

2.1.1 *Eigenmodes of Ideal Continuum Mechanical Structures*

In this section, analytical models are presented in order to describe the free and lossless vibration of continuum mechanical structures used as resonators. Beams and strings are 'one-dimensional' resonator examples. A string is a double clamped beam under tensile stress such that the tensile stress effect dominates over the beam's bending stiffness, so the main difference between a beam and a string is in

the way potential energy is stored: in beams it is stored in the elastic bending, while strings store potential energy in the work experienced against the strong tensile stress during deflection.
The starting point for deriving the eigenmodes of a continuum mechanical resonator is the Newton's third law, where all the forces acting on an infinitesimal piece of the structure are equalized.

2.1.2 *Doubly clamped beam*

One-dimensional bending vibration of doubly clamped beam (shown in Fig. 1) is one of the cases that can be exactly solved. The first assumptions to be taken into account to model the bending behaviour of a beam are that the beam is slender ($L/h > 10$) and that the rotational inertia and the shear deformation can be neglected. Starting from the Newton's third law applied to an infinitesimal piece of beam, the equation of motion of a beam can be derived.

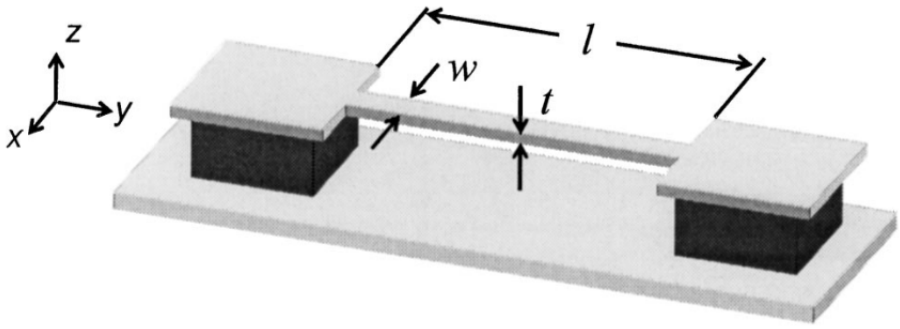

Figure 1: Doubly clamped beam resonator [15]

$$\rho A \frac{\partial^2 u(x,t)}{\partial t^2} = -EI_y \frac{\partial^4 u(x,t)}{\partial x^4} \tag{1}$$

where ρ is the mass density, A is the cross section, E is the Young's modulus, I_y the geometric moment of inertia with respect the y axis and $u(x,y)$ is the transient dispacement function. Again, to solve equation 1, the displecement function is seperated in space and time terms as follows

$$u(x,t) = \sum_{n=1}^{\infty} U_n(x) \cos(\omega t) \tag{2}$$

being $U_n(x)$ the spatial displacement function for the *eigenmode* with the number n and ω the angular velocity. A general solution of equation 2 can be written as

$$U_n(x) = a_n \cos \beta_n x + b_n \sin \beta_n x + c_n \cosh \beta_n x + d_n \sinh \beta_n x \tag{3}$$

where the two trigonometric function terms represent the standing waves in the center of vibrating beam and the two hyperbolic ones describe the behaviour of the clamping at the ends of the beam. β_n represents the *wavenumber*.
Considering as boundary conditions the fact that both the displacement and its slope are nill at the two ends of the beam because of the clamping, one can write

$$U_n(0) = U_n(L) = -\frac{\partial U_n(0)}{\partial x} = -\frac{\partial U_n(L)}{\partial x} = 0 \tag{4}$$

and, defining $A_n = b_n = -d_n$ and $B_n = -a_n = c_n$, equation 3 can be simplified as

$$U_n(x) = A_n(\sin\beta_n x + + \sinh\beta_n x) - B_n(\cos\beta_n x + \cosh\beta_n x). \tag{5}$$

Moreover, only a certain discrete set of specific wavenumbers β_n corresponding to the specific eigenfrequencies satisfy the boundary conditions so that

$$\cos(\beta_n L)\cosh\beta_n L = 1 \tag{6}$$

The previous equation can be graphically solved for the lower order modes, as shown in figure 2.

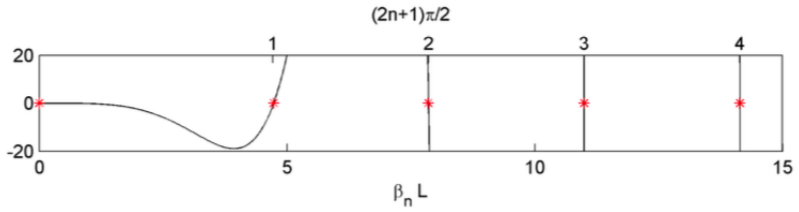

Figure 2: Graphical solution of equation 6 [16]

Non-trivial numerical solutions show that the $(2n+1)\pi/2$ approximation fit in a very good way all the first *wavenumbers*. The fundamental mode gives $\beta_n L = 4.730041$. At this point, the dispersion relation showing the dependence of a specific eigefrequency results putting the solution 5 into equation 2 and inserting this into the Euler-Bernoulli (equation 1):

$$\Omega = \omega = \beta_n^2\sqrt{\frac{EI_y}{\rho A}}. \tag{7}$$

In the case of width to height ratio higher than 5, also the transverse deformation of the beam has to be taken into account, so the flexural rigidity of the beam D_b turns into the flexural rigidity of a plate D_p

$$D_b = \frac{Et^2}{12} \rightarrow D_p = \frac{Et^2}{12(1-\nu^2)} \tag{8}$$

where ν is the Poisson's ratio, so that the *eigenfrequency* can be avaluated as

$$\Omega = \omega = \beta_n^2 \sqrt{\frac{D_p}{\rho t}} = \beta_n^2 \sqrt{\frac{Et^2}{12\rho(1-\nu^2)}}. \tag{9}$$

The boundary conditions can be used at x=L in order to calculate the ratio between the two coefficients of the displacement function $U_n(x)$.
From these results, the shapes of the modes of this kind of structure can be evaluated, having deflection for the first 4 Eigenmodes as shown in figure 3

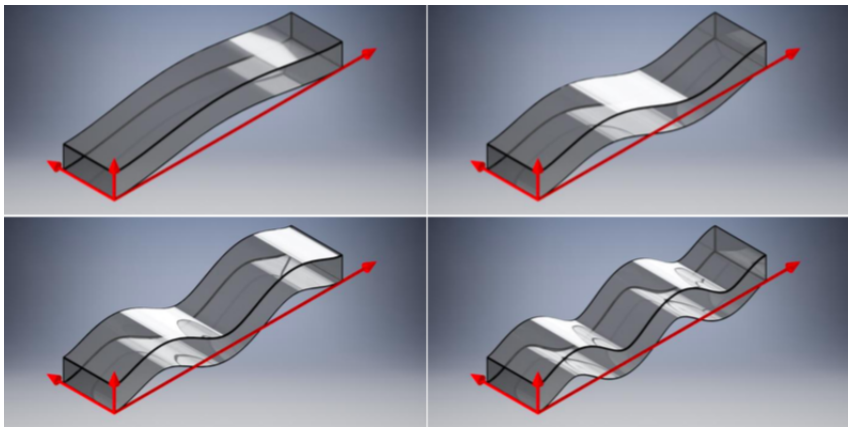

Figure 3: Deflected doubly clamped beam for the first 4 flexural modes [16]

2.1.3 *Pre-stressed beam*

Usually in MEMS applications, sensors are built of thin films, tipically deposited at very high temperatures leading thus to internal stress due to the fact that different materials are characterized by different thermal expansion coefficients (i.e. the bulk and the deposited materials). In order to take into account this stress, in the beams theory an force term representing this tensile force is added. This leads equation 1 to become

$$\rho A \frac{\partial^2 u(x,t)}{\partial t^2} + \frac{\partial^2}{\partial x^2}\left(EI_y \frac{\partial^4 u(x,t)}{\partial x^4} - F_x U(x,t)\right) = 0 \tag{10}$$

where F_x is the normal force within the beam. Exploiting the same assumption for the dispacement function U (equation 2) and considering a sinusoidal mode shape, the dispartion relation can be evaluated from equation 10, leading to

$$\Omega^2 = \omega^2 = \beta^4 \left(\frac{EI_y}{\rho A} + \frac{\sigma}{\rho \beta_n^2}\right) \tag{11}$$

That can be adjusted as

$$\Omega = \beta_n^2 \sqrt{\frac{EI_y}{\rho A}} \left(1 + \sqrt{\frac{\sigma A}{EI_y \beta_n^2}}\right) \tag{12}$$

resulting the *Eigenfrequency* to be dependent on two terms. The out of brackets term is the ideal beam one (equation 7), while the first term in the brackets is the *beam-like term* and the second one the *string-like term*. Using again the boundary conditions for doubly clamped beam (4) on the current sinusoidal displacement function, it can be found

$$\beta_n = \frac{n\pi}{L}. \tag{13}$$

The obtained results can be substituted into equation (12) giving two different cases for the *Eigenfrequency*:

- stiff, short and low-stressed beams for which the beam-like properties dominates the reosonant behaviour if

$$\sqrt{\frac{\sigma A L^2}{n\pi E I_y}} \ll 1 \tag{14}$$

- the flexural rigidity can be instead neglected leading the beam to behave like a string if

$$\sqrt{\frac{\sigma A L^2}{n\pi E I_y}} \gg 1. \tag{15}$$

In the first case, equation (12) turns into equation (7) while the *Eigenfrequency* related to a string-like beam can be simplified to:

$$\Omega_{string} = \frac{n\pi}{L} \sqrt{\frac{\sigma}{\rho}} \tag{16}$$

However, in order to obtain more precise results, the dispersion relation (11) has to be solved by taking into account in the displacement function also the clamping influences. With this consideration, the displacement function becomes:

$$U_n(x) = \sin \beta_\sigma x - \frac{\beta_\sigma}{\beta_E} \left(\cos \beta_\sigma x - \cosh \beta_E x + \sinh \beta_E x \right) \tag{17}$$

where $\beta_\sigma = \frac{n\pi}{L}$ is the *modenumber* of a perfect string-like behaviour and $\beta_E = \sqrt{\frac{\sigma A}{EI_y}}$ is related to the flexural rigidity of the structure.

2.1.4 *The Rayleigh method*

Until now the fundamental Euler-Bernoulli equation is derived starting from the Newton's third law, considering all the forces acting

on a differential element of the structure. This leads to get exact solutions for an idealized mechanical system. For studying more complex structures, is should be better to find the exact solutions of the previous equations. An useful tool exploited to obtain good approximated fundamental eigenfrequency of a conservative (ideal) system is the Rayleigh's method. This is based on the equipartition method, that states that the maximal kinetic energy $W_{kin,max}$ must be equal to the maximal potential energy $W_{pot,max}$

$$W_{kin,max} = W_{pot,max} \tag{18}$$

In order to calculate the enrgies, the specific mode shape of the structure $u(x,y,t)$ is required that, separating the spatial and temporal variables, can be written as

$$u(x,y,t) = U(x,y)\cos(\omega t) \tag{19}$$

where the temporal sinusoid modulates the spatial mode function $U(x,y)$ with a certain angular velocity ω [17].
Being the maximum value of a sinusoidal function equal to 1, the maximum potential energy results to be

$$W_{pot,max} = max\{W_{pot}(u(x,y,t))\} = W_{pot}(U(x,y,t)). \tag{20}$$

Since the kinetic energy is

$$W_{kin} \propto \left(\frac{\partial u(x,y,t)}{\partial t}\right)^2 \tag{21}$$

and taking 19, the maximal kinetic energy can be written as

$$W_{kin,max} = \omega^2 W_{kin}(U(x,y)). \tag{22}$$

Substituting 20 and 21 in 18, the eigenfrequency Ω of a specific eigenmode is

$$\Omega^2 = \omega^2 = \frac{W_{pot}(U(x,y))}{W_{kin}(U(x,y))} \tag{23}$$

The exact eigenfrequency can be obtained only if the mode shape is exactly known, but usually the mode shape function can be just approximated, by satisfying the right boundary conditions.
Considering a clamped beam, equation 23 can be exactly calculated:

$$\omega^2 = \frac{W_{pot}(U(x,y))}{W_{kin}(U(x,y))} = \frac{\frac{1}{2}EI_y\int_0^L\left(\frac{\partial^2 U}{\partial x^2}\right)dx}{\frac{1}{2}A\rho\int_0^L\left(\frac{\partial U}{\partial t}\right)dx} = \left(\beta_n^2\sqrt{\frac{EI_y}{\rho A}}\right)^2 \tag{24}$$

If the mode shape function $U(x)$ is not known, the displacement function is assumed under constant load leading to an overstimation of the *Eigenfrequency* so that the *Eigenmode* is instead at smaller value.

2.1.5 *Damped Linear Resonator*

Taking into account the dissapitive effects in real MEMS devices, a lumped-model is introduced. In this way, the fact that the energy exchange between kinetic and potential one is characterized by losses is considered. This dissipation happens through internal dampening mechaninsm so that, at the end, the resonator is no more vibrating exactly at the *Eigenfrequency* but at its *resonance frequency*, resulting close to, but a little lower than the actual *Eigefrequency*.
Thus, the lumped-model contains a massless spring describing the idealized lossless system and a dashpot put in parallel for the dissipative effects, both connected to a poit mass, as schematized in fig. 4.
A differential equation with the assumption of small amplitudes can

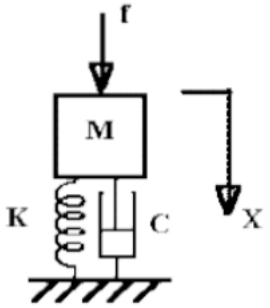

Figure 4: 1D lamped model of a damped resonator with a spring and a dashpot connected to a mass [18]

be used for expressing this 1D model of the resonator with a point mass at a certain deflected point:

$$M\frac{\partial^2 z}{\partial t^2} + C\frac{\partial z}{\partial t} + Kz = f(t), \tag{25}$$

with M the effective mass of the resonator, C the dampening coefficient of the dampener, K the spring constant and $f(t)$ the excitation force.

2.1.5.1 *Free Undumped Vibration*

In the case of a non-driven lumped-element resonator with no damping ($C = 0$), the energy of the system is kept constant, so the resonator behaves like an oscillator characterized by a vibrational amplitude $z(t) = z_0 \cos(\omega t)$. During a period of oscillation, the energy is completerly exchanged between kinetc and potential energy and following again the equipartition theorem, the two energies have to be the same:

$$\frac{1}{2}M\frac{\partial^2 z}{\partial t^2} = \frac{1}{2}Kz^2 \tag{26}$$

giving as *eigenfrequency* of the undamped system

$$\Omega = \omega\sqrt{\frac{K}{M}} \tag{27}$$

2.1.5.2 *Free Damped Vibration*

In this situation, equation (25) comes into a homogeneous differential equation

$$\frac{\partial^2 z}{\partial t^2} + 2n_c\frac{\partial z}{\partial t} + \Omega z = 0 \tag{28}$$

where $n_c = \frac{C}{2M}$ is the damping coefficient. By putting in equation (28) a trial solution $z = z_0 e^{\gamma t}$, it gives solutions that satisfy

$$\gamma_{1,2} = -n_c \pm i\sqrt{\Omega^2 - n_c^2}. \tag{29}$$

The *dampening ratio* is defined as the ratio between and the damping coefficient and the eigenfrequency and gives information about the system performances:

$$\zeta = \frac{n_c}{\Omega} \tag{30}$$

Depending on the ζ value we can have different solitions:

- $\zeta \geqslant 1$, so γ is real and the solution of (29) is an exponential decay. This is the over-damped case, in which the system is heavily damped.
- $\zeta < 1$, so γ is imaginary. This is the under-damped case, in which the system is slightly damped.

By applying the Euler formula, the solution of equation (28) can be written as:

$$z(t) = z_0 e^{-\Omega\zeta t}\cos\left(\Omega\sqrt{1-\zeta^2}t\right). \tag{31}$$

This final equation shows an exponential decay of the oscillation whose trend is shown is Figure 5 with a frequency called *natural frequency* $\omega_n at = \Omega\sqrt{1-\zeta^2} = \sqrt{\Omega^2 - n_c^2}$. In order to understand the performance of a resonator, an important rule is given by the *Quality factor* of the system. The quality factor indicates the sharpness of the resonance peak. Physically it is defined as the ratio between the stored and lost energy during one cycle at resonance

$$Q = 2\pi\frac{W}{\Delta W} = \frac{M\omega}{C} = \frac{\sqrt{1-2\zeta^2}}{2\zeta} \tag{32}$$

with W the total energy stored in the system and ΔW the energy lost in one oscillation cycle.
In this case, the Quality factor can be written as

$$Q = \frac{1}{2}\Omega\tau \tag{33}$$

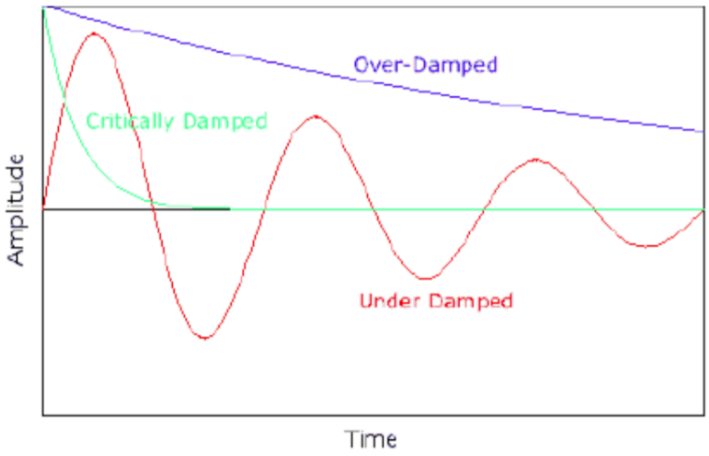

Figure 5: Plot of 31 [18]

where τ represents the time at which the amplitude of the vibration reaches $1/e$ if the initial amplitude.
Assuming for the previous lamped model a sinusoidal force $f(t) = f_0 \sin \Omega t$, gives as solution of equation (28) the sum of the harmonic differential equation (free damped vibration (5)) and a specific steady solution:

$$z(t) = z_0 e^{i\omega t} \tag{34}$$

that can be written in its polar coordinates as

$$\|z_0\| = \frac{f_0}{M\sqrt{(\Omega^2 - \omega^2)^2 + 4\zeta^2\Omega^2\omega^2}} \tag{35}$$

$$\varphi = \arctan\left(\frac{2\zeta\Omega\omega}{\omega^2 - \Omega^2}\right) \tag{36}$$

where z_0 is the amplitude of vibration and φ the phase between the excitation and the response of the resonator.
Another important parameter is the dynamic gain, defined as the ratio between the maximum vibrational amplitude of the excited resonator and the deflection due to a static force:

$$\begin{aligned}\delta(z_{0,max}) &= \frac{\frac{f_0}{M}}{\sqrt{(\Omega^2 - \omega_r^2)^2 + 4\zeta^2\Omega^2\omega_r^2}} \Big/ \frac{f_0}{K} = \\ &= \frac{\Omega^2}{\sqrt{(\Omega^2 - \omega_r^2)^2 + 4\zeta^2\Omega^2\omega_r^2}}\end{aligned} \tag{37}$$

with ω_r is the *resonance frequency* where the peak of δ is put, so that:

$$\frac{\partial\delta(\omega)}{\partial\omega}\Big|_{\omega=\omega_r}. \tag{38}$$

Putting together equations (37) and (38) the resonance frequency can be obtained:

$$\omega_r = \Omega\sqrt{1 - 2\zeta^2}. \tag{39}$$

The convergence of the resonance peak towards the *Eigenfrequency* value increases for small dampening factors and, furthermore, the peak of the amplitude response increases with the quality factor.

2.1.6 *The Quality Factor*

Several dissipating effects play a role In the evaluation of the Quality factor, being that a measure of the how much energy is lost in the resonator during a vibration cycle with respect to the total stored one. For this reasone, the quality factor can be seen as the sum of different components, each related to different dampening contributions. As can be seen from equation (40), the main dampening effects contributing to the quality factor are:

- the intrinsic dampening in the resonator material
- the dissipation present in hte clamping areas of the system
- the dampening induced by viscous effects, such as air in the resonator.

$$\frac{1}{Q} = \frac{1}{Q_{intrinsic}} + \frac{1}{Q_{clamping}} + \frac{1}{Q_{viscous}} + ... \tag{40}$$

For high quality factor resonators, the air contribution results to be the dominating one and it can be easily removed by operating in vacuum conditions. However, the liquid inside the resonator still dissipates part of the mechanical energy, leading to a reduction of the Q factor.
The evaluation contribution of the liquid can be very complex: the energy dissipation depends on both the mode number [19] and the Poisson's ratio [20].
In hollow structures, the Q factor results to decrese with the mode number. In particular, some acoustic dissipation effects are present when the cavity is located away from the neutral axis of the resonator leading to the so called "pumping effect" resulting in fluid compressibility. These effects do not affect the fundamental mode and show an increasing role for higher mode numbers.
Furthermore, in smaller devices (low inertia) a shear driven mechanism leads to the rise of the energy dissipation with increasing the viscosity of the fluid, thus making these devices typically more susceptible to the increasing dampening effects of higher mode numbers. These effects result to be reversed for high viscosity samples because here the dampening boundary layers overlap for higher modes, so the energy dissipation results to fall down with the viscosity rise.
Also the Poisson's ratio strongly affects the resonator behaviour. In particular, the magnitude of the flow induced in the channel by the cross sectional compression is strongly influenced by the Poisson ratio when the channel is put off the neutral axis. The flow is strickly

related to the energy dissipation and so to the Quality factor of the system.
Considering the a cylindrical channel geometry, it comes out that there is a low influence of the viscosity of the sampe on the Q factor of the system.
The channel is placed close to the neutral resonator axis and the system works at the fundamental resonance mode. Furthermore, the Poisson's ratio of both SRN and silicon is around 0.27, so relatively large, and the cross section is minimized in order to maximize the sensitivity of the resonator. All these considerations, will likely lead to a resonator quality factor highly dependent on the sample viscosity.

2.2 READOUT AND ACTUATION

In this section an overview of the mechanisms, the actuation and readout principles exploited is given. After, an introduction to Allan Deviation for quantifying the noise components of the resonators and the applied readout mechanisms is presented.

2.2.1 *Actuation principles*

When a mechanical system is above the absolute temperature it vibrates ar its resonance frequency, due to thermal effects. This results a thermomechanical noise, whose amplitude is given by the following equation:

$$S_{x,ThMech}(f_0) = \frac{k_B T Q}{2\pi^3 M f_0^3} \tag{41}$$

where T is the absolute temperature, M the effective mass of the resonator, f_0 the resonance frequency and k_B the Boltzmann constant.

2.2.2 *Readout principles*

Several methods can be implemented for the detection of the motion of a resonator [21]. Generally, there are two main classes present in the literature: optical and non-optical readout methods. Different readout methods exist for the non-optical ones:

- Piezroresistive, exploiting the modulation of the resistance of piezoresistive gauges due to the strain introduced by the resonator motion;
- Piezoelectric, inducing a voltage thanks to the strain induced by the resonator deflection;
- Capacitive, where the position of the plates of the capacitor changes due to the resonator movement;

- Magnetomotive, in which a strong magnetic field generates an electromotive force on a conducto posioned on top of the resonator, resulting in an potential variation.

Regarding all, some modifications of the fabrication process of the resonator in order to be applied, as well as an electronic interfacing.
On the other hand, for the optical methods a clear line of sight is required leading to introduce a laser beam on the resonator surface. This results sometimes very challenging. The main optical mechanisms are:

- Optical lever readout, that focuses a laser beam on the resonantor leading to experience an angular displacement;
- Interferometric readout, using commercial LDV or Michelson and Fabri-Perot interferometers;
- Astigmatic readout, where the astigmatic autofucus is used to monitor the motion of the resonator.

In this work, the interferometer readout is exploited, using a Laser Doppler Vibrometer, whose working principle is explained in section 5.1.1. This is characterized by an extremely low spectral density noise and by a high responsivity. Indeed, displacement detection through this kind of method is enhanced by decreasing the dimensions of the device, allowing to obtain ultrasensitive displacement detection [22] . For this reason the interferometric optical one is used as reference method to be compared with the results obtained from the others.

2.2.3 *Allan Deviation*

In order to measure the stability of the resonance frequency of a resonator, a real-time monitoring of it is performed by implementing a PLL to track the phase and consequently also the frequency detuning over time.
For a MEMS resonator, it is not enough to give the spectral noise density at 1Hz, since the resonance frequency usually does not convenrge over time. A longer averaging time, indeed, can not lead to a more precise measurements due to the frequency drift induced by temperature. To characterize A MEMS resonator the *Allan Deviation* (AD) is measured [23] [24].
The Allan deviation is defined as one half of the time average of the squares of the differences between samples and so it results to be dependent on the sample period [25]. It can be interpreted as the minimum resolvable relative shift of frequency for a certain integration time τ. Furthermore, the evaluation of the AD indicates the limiting noise components nature. As it can be seen in figure 6, two different factors limit the integration times at two different regimes: at low integration times, the white noise is the dominating limiting factor, whose

trend is $\propto \tau^{-1/2}$, while for long averaging times, the frequency shift dominates ($\propto \tau$).

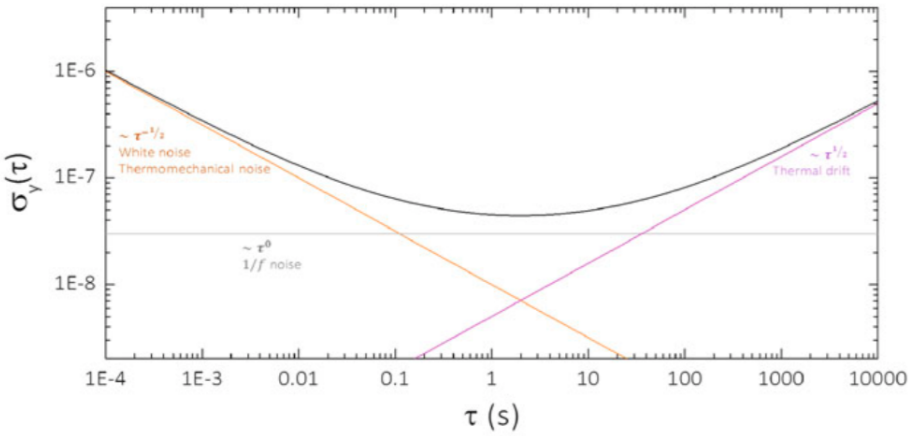

Figure 6: Typical Allan Deviation plot as a function of the integration time [14]. The black line shows the overall Allan deviation composed of three contributions (in this particular example): white and thermomechanical noises (yellow line), the 1/f noise (grey line) and the drift or random walk noise (pink line).

2.3 THEORETICAL ANALYSIS

Now the expected responsivities and sensitivities of the developed sensor are calculated.

2.3.1 *Minimum resolvable frequency shift*

The practically measurable minimum frequency shift that determines the detection limits of a resonator MEMS sensor can be measured with the AD. The minimum resolvable relative frequency shift is determined by the theoretical limit of the signal to noise ratio and the resonator Q factor:

$$\delta f_{min} = \frac{1}{2Q\ SNR} \tag{42}$$

2.3.2 *Density and Mass sensitivity*

One of the main advantages of hollow resonators is the ability to do precision measurements on liquid samples.
The previously explained formuals for the evaluation of the eigenfrequency of a pre-stressed resonator sensor can be rearranged in order to evaluate density and mass responsivities of the resonator itself. Indeed, in equation 12 the eigeinfrequency results dependent on the resonator density, that should so take into account also the contribu-

tion of the sample density when filled with it. This means that the relative frequency shift is fundamentally coupled to the relative mass shift of the resonator and so on the sample density.
The sample density responsivity can be easily found by calculating the derivative of the resonance frequency with respect to the density of the sample, obtaining:

$$R_{\rho_{sample}} = \frac{\partial \Omega}{\partial \rho_{sample}} \propto -\frac{V_{sample}}{2V_0\sqrt{(\frac{m_0+\rho_{sample}V_{sample}}{V_0})^3}} \tag{43}$$

Where V_0 is the combined volume of the resonator and sample channel and m_0 the mass of the empty resonator.
More important is however the smallest resolvable density change $\Delta\rho_{min}$ of a given sample resulting directly proportional to the smallest relative frequancy shift, δf_{min}.
Another goal of the project is to develop a sensor able to perform mass spectroscopy on the massrange of single yeast cells in a growth media. As a starting point, the equation for calculating the Eigenfrequency of a lumped-model oscillator is used (equation 27). The squares of the Eigenfrequency Ω_0 and Eigenfrequency with an added mass $\Omega_{\Delta m}$ are sutracteed:

$$Omega_0^2 - \Omega_{\Delta m}^2 = \frac{k_eff}{m_eff + \Delta m} - \frac{k_eff}{m_eff} \tag{44}$$

This can be solved fot the added mass Δm:

$$\Delta m = m_{eff}\left(\left(\frac{\Omega_{\Delta m}}{\Omega_0}\right)^{-2} - 1\right) \tag{45}$$

By introducing the relative frequency shift induced by the added mass $\delta\Omega_m$, this results in:

$$\Delta m = m_{eff}((\delta\Omega_{\Delta m})^{-2} - 1),\ with\ \delta\Omega_{\Delta m} = \frac{\Omega_{\Delta m} - \Omega_0}{\Omega_0} \tag{46}$$

This equation can be used to evaluate the mass of a particle on the resonator under the assumption that the particle is located in a spot with the maximum amplitude of the resonator displacement function.
Considering

Part II

SIMULATION

3

FINITE ELEMENT METHOD ANALYSIS

In this chapter the results and the discussion on the simulation work carried out using COMSOL Multiphysics are collected. The software is based on the Finite Element Method (FEM) applied to the designed resonator geometry. The FEM approach operates subdividing the system under study into small units (*finite elements*) interconnected at points common to two or more elements (*nodes*) and/or boundary lines or surfaces. Through this method, the equations are solved for each finite element assuming that each physical quantity varies linearly and the obtained solutions are then combined to get the whole body one [26]. In order to find the minimum energy configuration of the system, the software lets the quantities vary in each node starting from appropriate boundary conditions provided by the user [27].

The goal of this section is to simulate and understand the resonance behaviour of the resonator by modelling the system in the simplest way possible. In particular, through this software a mechanical Eigenfrequency analysis is performed. When vibrating at a certain eigenfrequency (descrete frequencies at which the system is prone to vibrate), a strucutre deforms into a corresponding specific eigenmode, representig the shape of the vibration. An eigenfrequency analysis is able to only provide the shape of the mode, not the amplitude of the real physical vibration. The true size of the deformation can only be obtained knowing the actual extication together with the damping properties of the considered system[28].
It is important to underline that in these simulations, although no dissipative effects are taken into account, the resulting resonance frequencies give a very good idea of the actual ones

3.1 COMSOL IMPLEMENTATION DESIGN

An overview of the specifications used to model the resonator is presented in this part of the chapter. In particular, starting from the assumptions exploited to simplify the geometry of the structure, then the materials mechanical properties are discussed and finally the boundary conditions exploited.

3.1.1 *Model simplification*

In order to keep the number of elements not so high in the simulation, the SCR channel shape is simplified. This means that the entire sys-

tem is built by means of simple solid primitive 3D components - the lowest number as possible - and by maintaining the cross section area of the resonator constant while the channel one varying only in the central part symmetrically with respect to the center of the structure.

Furthermore, both the liquid and the immuno cell inside the channel are modeled as solids by only setting the proper mechanical properties - Young's moduli, Poisson ratios, densities - in order to ensure stable simulations and to not influence significantly the evaluated eigenfrequencies. The cell is simply modeled as a perfect sphere or a regular ellipsoid and the silicon etching during the channel shaping is considered as ideally isotropic, leading to a final channel cross-section perfectly circular.

To simulate the resonance frequency of this kind of strucutre, *Solid Mechanics* physics is used, in an *Eigenfrequency* study. To reach this aim, the residual stress needs to be assigned assuming a linear elastic behaviour of the materials and it is put equal to $\sigma = 220 \cdot 10^6$ N/m^2. Indeed, to estimate the sensor behaviour, it is importa to take in consideration this factor, since the residual stress in the SRN reduces the significance of the resonators flexural rigidity and geometry in general.

3.1.2 *Geometrical implementation*

As a starting point for the simulation implementation, the system is designed based on the measuremement results obtained through the SEM analysis performed during the fabrication processes, described in chapter 4 and discussed in section 6.1.2.
In Table 1 the main parameters of the structure are shown.

Table 1: List of the geometrical parameters used in this simulation.

GEOMETRICAL QUANTITY	VALUE
Total channel length	514 µm
Length of the constant-section half channel	245 µm
Length of the central central part of the channel	24 µm
Channel radius	12 µm
Central hole radius	5 µm
SRN thickess	500 nm

The final structure results in a SRN hollow cylinder 500nm thick, whose radius is kept almost constant at 11.5µm along the entire microchannel, exept for the central part that is designed in order to stop the

cell thus showing a lower central radius equal to 4.5µm.
The structure is entirely closed by a SRN layer 500nm thick and 40µm wide. Considering that the etched silicon depth in an isotropic etching profile can be approximated as 5/3 of the radius, the latter is set as 12µm in order to get a depth equal to nearly 20µm, being the actual value observed during the fabrication steps equal to about 19µm (see section 6.1.2). The basic geometrical design is shown in Figure 7.

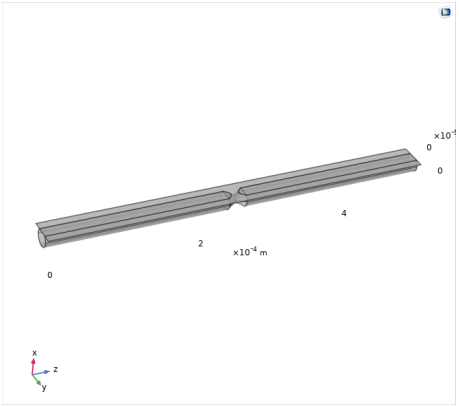

Figure 7: COMSOL geometrical design

To have a more realistic design, it has to be considered the fact that during the final isotropic Silicon etching process for the realease of the resonator, due to the non constant cross-section in the central part of the channel, some residual Silicon is expected to be still present above the central part of channel. This extra-mass can affect the final frequency behaviour of the resonator and for this reason needs to be taken into account also in the simulation step. The residual Silicon mass is characterized by a very irregular 3D shape and a no simply predictible volume, since both are affected by several factors during the isotropic etch process. In order to keep the geometrical design of the structure as simple as possible, the residual Silicon mass is modeled as a regular pyramid whose base is directly connected to the top SRN layer and apex pointing down, towards the channel, as shown in Figure 8.

Also the cell and the liquid inside the channel are modeled as solids in order to get stable simulation results. In particular, the water is designed as a solid perfectly filling the whole structure, while the cell shape and dimesion are set starting from experimental data, showing an estimated mean diameter uqual to 14.1µm, also confirmed in the literature [29] even if their shape results to be quite irregular and characterized by the presence on the surface of some microvili of different length [30].

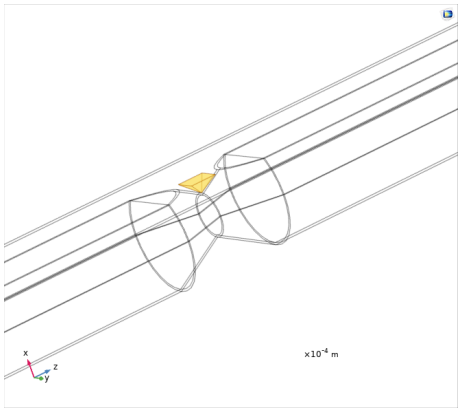

Figure 8: COMSOL residual silicon geometrical design

3.1.3 *Materials definition*

As previously said, in these simulations, everything is designed as a solid, also cell and the fluid inside the channel. In particular, each domain needs to be defined in its own material. The SRN for the entire resonating structure, so channel plus the closing layer, and the silicon for the residual volume are taken from the material library of the software, with all the properties already defined. For the fluid instead the water is considered and so a new material needs to be introduced, giving to it the main mechanical properties, in particular density, Young's Modulus and Poisson's ratio. This is done by fillng the whole channel with a 3D component with the same shape and giving to that component the required mechanical properties; specifically, water Young's modulus is assumed equal to 1GPa in order to ensure stable simulations and moreover to not influence too much the evaluated eigenfrequencies. The same is done for the cell, adding a further more material characterized by the same properties of water, except that for its density, being it a little higher. The materials exploited and their properties are shown in table 2.

Table 2: Material properties assumed for the simulations

	Material			
Property	SRN	Silicon	Water	Cell
Density (kg/m^3)	2800	2330	997	1100
Young's Modulus (GPa)	240	170	1	1
Poisson's ratio	0.27	0.28	0.23	0.23

3.1.4 *Boundary Conditions*

Once the geometry and the materials are defined, the boundary conditions can be set. In particular, the SCR structure is modeled in such a way to constrain the displacement of each point on the external surfaces of both the channel and the closing SRN layer to be zero in all directions. This is done by simply selecting the *fixed constraint* condition on the mentioned surfaces. Also the residual stess is set to a value of $220 \cdot 10^6$ Pa.

3.2 SIMULATION RESULTS

In this section the results obtained from the different simulations are discussed.
In order to have a more detailed and realistic implementation, some features are varied, so as to be sure that the resonance behaviour of the structure is maintained.

3.2.1 *Parameter Variation*

One of the main issues of the simulation part regards the ability to design the structure in the most precise way possible. This is extremely challenging and important due to the fact that dealing with micro-sized structures means that a small variation in their mass can lead to an important variation from a resonance point of view. In particular, what results difficult to characterize is the volume of the residual silicon present on the narrower part of the channel (fig. 8). For that reason, the simulations are run for different volumes of this residual mass going from the minimum expected one of $5\mu m^3$ to the maximum of $40\mu m^3$, values that come from considering the worst and best cases of the isotropic etch rate during the release of the channel, with a step of $5\mu m^3$.
Another variation is performed on the shape of the cell. As previously explained, this results very irregular and furthermore strictly dependent on the cell cycle itself. What is done is to start from a fixed volume evaluated considering a sphere cell whose volume is the one coming form the regular sphere volume $V = 4/3\pi r^3$, with the diameter resulting from the experimetal mean equal to $14.1\mu m$. From this volume, six different elliploid shapes are simulated implementing six different semi-axis lengths. This is done in order to take into account the extention due to the presence of the microvilli on its surface. In fig. 9 the spherical shape is implemented, while in fig. 10 the ellipsoid shapes in which the semi-axis along the channel gets longer are shown. The implemented shapes are obtained varying the ratio between the direction along the channel and the other two direction according to the following values: $ratio = \{1.5,\ 2,\ 5,\ 4,\ 10\}$.

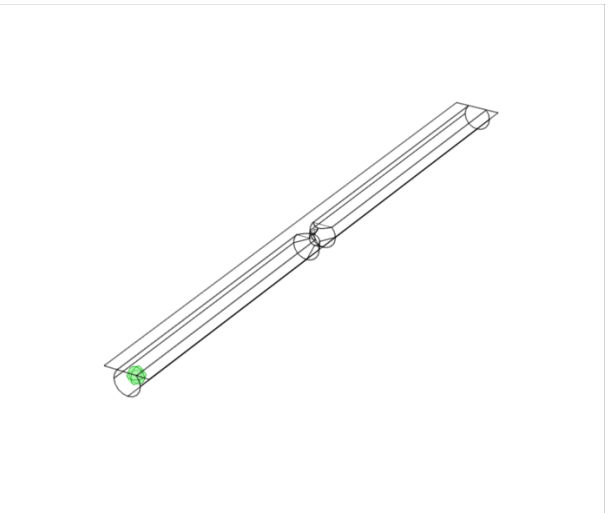

Figure 9: COMSOL structure of the SRC with a sphere cell shape characterized by a diameter of 14.1µm

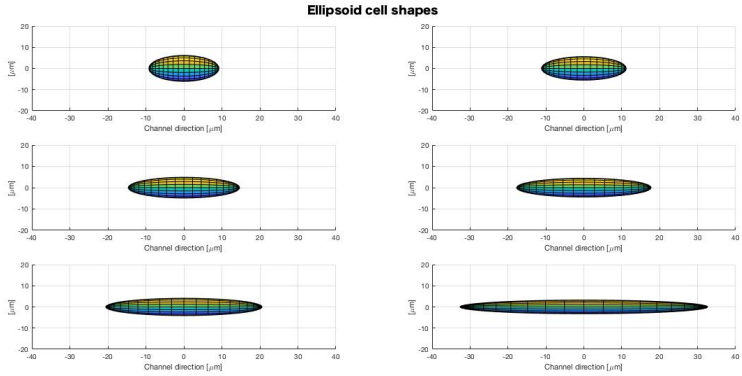

Figure 10: Different ellipsoid cell shapes simulated varying the ratio between the dimension of one semi-axis with respect to the others

3.2.2 *Results*

The simulations are run in two different steps in order to understand how the estimation of the eigenfrequency of the resonator varies by moving the cell along the channel.
A first simulation is run by moving the cell from outside the channel to the end point of it in 13 steps equally distributed. This is run for both the sphere and the rod cell shapes. In particular, in this part, the analysis is focused on the possible effect that the variations of the residual volume can lead to, so the only ellipsoid simulated is the extreme case, the one with the longest semi-axis (25μm).
In figures 11 and 12 the trends of the fundumental flexural mode are plotted for the sphere and rod cells respectively. In the upper plots there is the monitoring of the eigenfrequency, while in the bottom ones the normalization with respect to the starting value in ppm is shown, in order to understand how effective results the shift of the eigenfrequeuncy by moving the cell inside the channel.

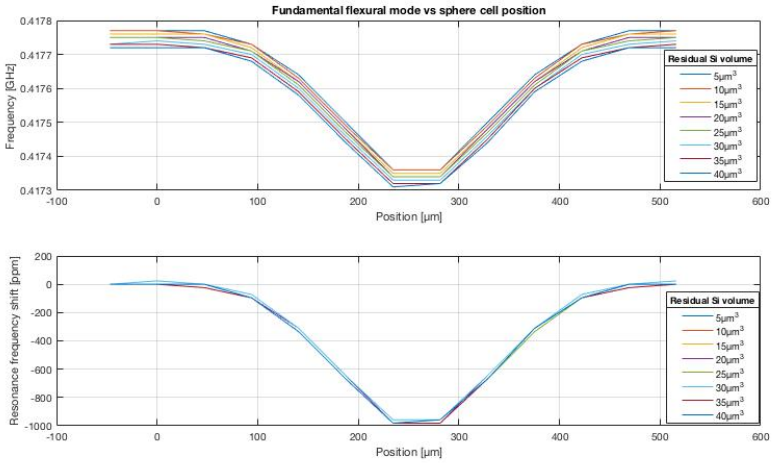

Figure 11: Shift of the fundumental flexural mode of the resonator with a sphere shape cell moving along the channel considering different residual silicon volumes

As it can be seen from the plots, the overall eigenfrequency in both cases - sphere and rod shapes - decreases with the increase of the volume of the residual silicon, as expected from the theory. Furthermore, even if there is this small difference, from the bottom plot it comes out that the realtive shift results to be quite the same for all the cases, reaching a value in the central points of the channel of $\sim$ 1000 ppm, ensuring that it does not really metter how much material is left after the channel is released since the responsivity (relative shift) measured stays largely the same.
Since the trends look kind of similar, it would help to show how the eigenfrequency values in the center varies with respect to the variation of the residual volume. In figure 13 the trends of the min-

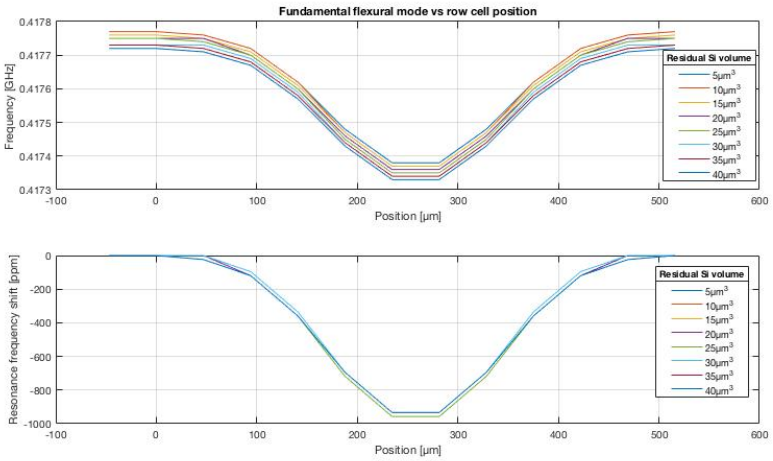

Figure 12: Shift of the fondumental flexural mode of the resonator with an rod shape cell moving along the channel considering different residual silicon volumes

imum eigenfrequency is plotted starting from the values extracted through the software and a third degree polynomial is then fitted on that points in order to extract a more clear trend. In both cases - sphare shaped (figure 13a) and row shaped (figure 13b) cells - the eigenfrequency results to linearly decrease with the increase of the residual volume, thus with the increase of the mass.

In the second step, some finer simulations are run, in which the number of positions of the cell inside the channel used to perform the analysis is increased from 13 to 52. In this case, the residual volume is kept fixed to the average value equal to $20\mu m^3$, but all the six shapes of the cell are simulated. All the results are shown in fig. 14.

Also in this case, the resulting trends are quite the same for all the structures, as expected, since there is no difference in masses. The only difference is in how the cell mass is distributed into the channel, but this is not so influencing on the vibrating state of the resonator. Again, the relative shift results close to ~ 1000 ppm, as in the previous case.

A promising behaviour of the sensor results from these simulations. Indeed, it comes out that also considering a noise contribution to the shift of ~ 100ppm, the designed SMR is able to show an appreciable shift (with a SNR > 10) in its fundamental flexural mode when the cell passes through it, moving from the external points ot the central one, that is actually where it should be detected. Furthermore, such a structure seems to be well performing in any of the variable cases taken into account, such as the cell exact shape and the actual volume of the silicon still present on the channel after the channel release step.

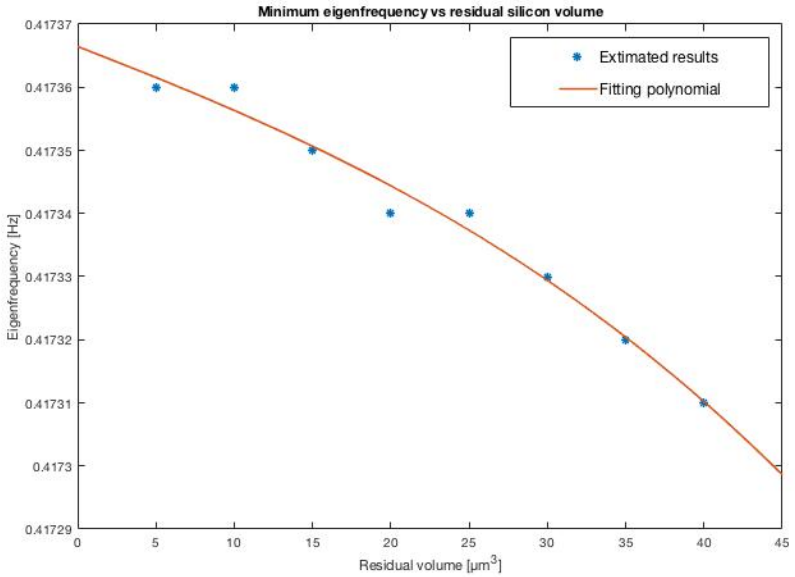

(a) Sphere shaped cell

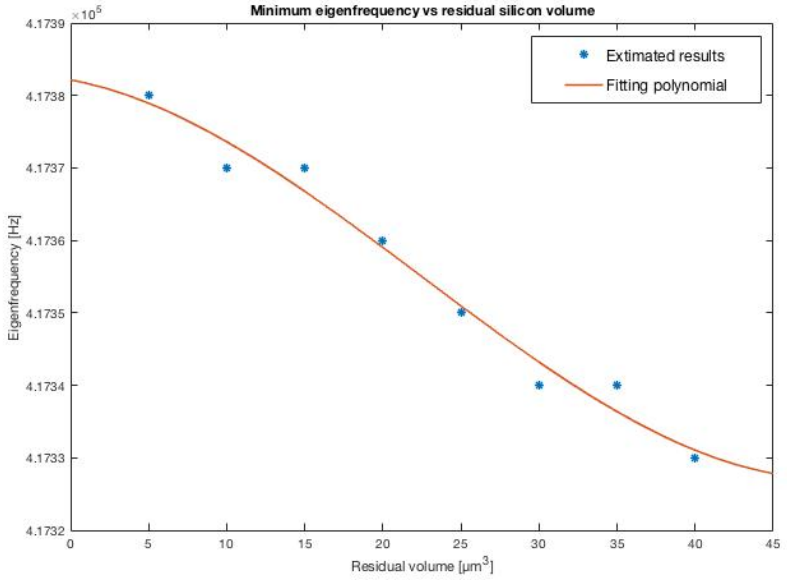

(b) Ellipsoid shaped cell

Figure 13: Variation of the fundamental flexural mode vs the volume of the residual silicon

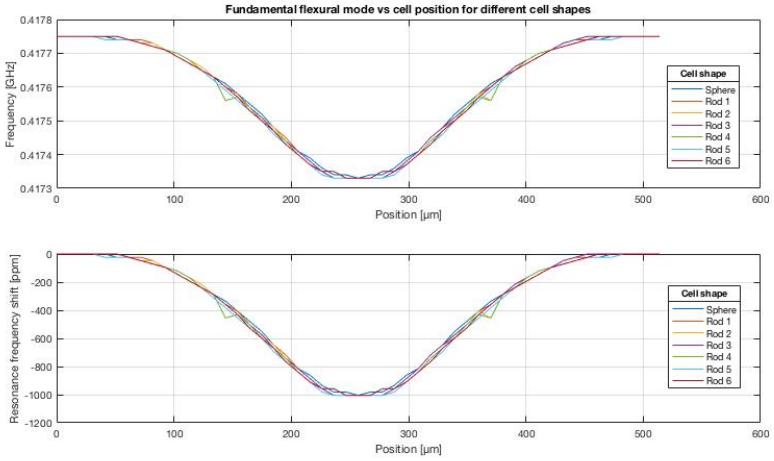

Figure 14: Shift of the fundumental flexural mode of the resonator with cell moving along the channel considering different shapes if the cell

Part III

MATERIALS AND METHODS

4

FABRICATION

The current chapter is focused on the detailed description of the fabrication processes exploited in order to obtain a versatile hollow MEMS sensor able to perform different kinds of measurements, such as mass/density spectrometry, viscosity and IR absorption spectroscopy. All the fabrication steps have been performed inside an ISO 5 standard 14644-1 (class 100) cleanroom location belonging to DTU Danchip, Denmark national micro and nano-fabrication center.

4.1 FABRICATION OVERVIEW

The main steps are schematized in figure 15. The starting point of the fabrication processes is a 4 inches silicon wafer 350μm think with a LPCVD SRN thin film of about 320nm on it (fig. 15a), where an array of slits is opened up on the wafer front side (fig. 15b). In order to get the fluidic access, vertical channels are etched through the whole wafer from the backside, ensuring the front side covered by a PECVD protective layer (fig. 15c). After that, the isotropic dry etch process through an array of slits created on the SRN masking layer is exploited to obtain the micro channel on the front side (fig. 15d). These slits are then closed by deposition of more SRN, leading to the formation of a SRN covered microchannel (fig. 15e). At the end, the SRN round is opened up and through another isotropic silicon etching process the SCR is released (fig. 15f, 15g).

4.2 FABRICATION TECHNIQUES

In this section a description of the physics of the main technological processes involved in the fabrication is given.

4.2.1 *Chemical Vapor Deposition*

Chemical vapor deposition (CVD) stands for a set of processes used in order to get the formation of thin film from vapor phase reactants (gaseous precursors). Through this techniques a wide range of materials can be deposited, going from metals to semiconductors to insulators.
The working principle of each kind of CVD is to involve an energy source to break reactant gases into reactive species for deposition [31]. As shown in Figure 16, in a CVD process, reactant species first diffuse to the substrate and then are adsorbed on its surface in order to de-

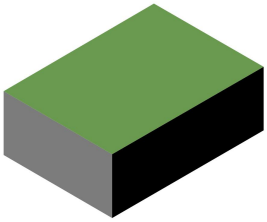

(a) Silicon wafer with LPCVD SRN layer

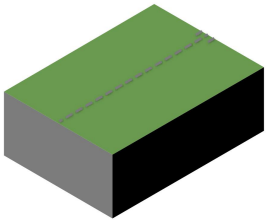

(b) Design of the pattern of the micro channel mic

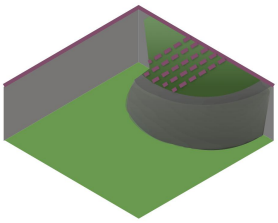

(c) Backside view of the access channel

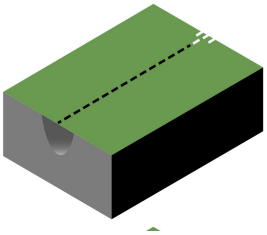

(d) Channel shaping after isotropic silicon etching

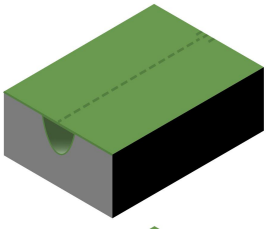

(e) Closing of the channel by means of LPCVD SRN deposition

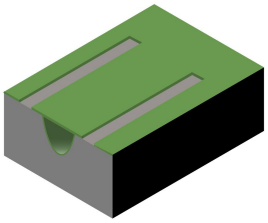

(f) SRN layer etched for the SCR release

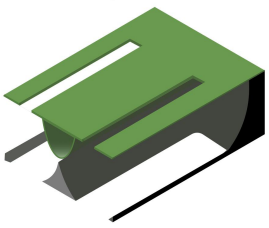

(g) SCR release with isotropic silicon etching

Figure 15: Scheme of the fabrication process steps [16]

position start. Then the reactive species can stay fixed at the surface site or they can move along the surface, depending on the working temperature. The reaction rate results to be thus strong dependent on the temperature, increasing with the temperature rise until a maximum limit value R_0 at which it saturates for very high temperature conditions as described by equation (47).

$$R = R_0 e^{-\frac{E_a}{k_B T}} \tag{47}$$

Depending on the working condition and on the energy source ex-

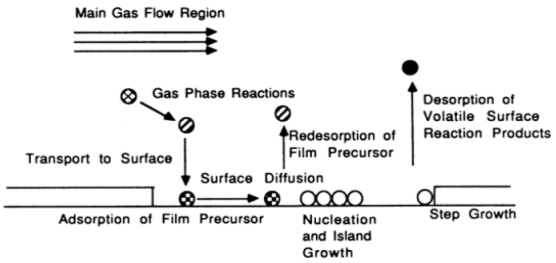

Figure 16: Chemical Vapor Deposition working principle scheme

ploited to activate the chemical reactions, several CVD tecnhiques can be carried out. In this project, two are the main ones used that will be described in detail:

1. Low Pressure CVD, characterized by a working pressure lower than the atmospheric one, ranging between $5Pa - 250Pa$. The low pressure leads to a better uniformity of the deposited film thanks to the longer mean free path of the reactants, while the relative lower working temperature reduces the dopant diffusion. These advantages, however, decrease also the reposition rate and require a more expensive pumping equipment. The available furnace used in this process is the Tempress LPCVD nitride furnace, used in particular for low stress silicon nitride deposition.

2. Plasma Enhanced CVD, in which plasmas are used to force reactions that would not be possible at low temperature, thus giving the energy required to generate the reactive gases. This allows to work at lower temperatures ($225°C - 450°C$) and to have more degrees of freedom to achieve film properties, as good step coverage, density and composition. The main disadvantage of the Plasma Enhanced CVD is the damage or the chemical contamination that can be done through the plasma. The equipment exploited in this project is the SPTS Multiplex PECVD system working at a temperature of 250°C and 300°C for the top and bottom electrodes rispectively.

4.2.2 *Optical photolithography*

Photolithography is the process exploited in microfabrication to transfer the desired pattern from a mask representing the master copy of the design into a polymer layer, the photoresist, on the wafer surface [32]. The polymer is so patterned and used as a protective layer of the wafer areas that have not to be etched. Through this technique, the circuit element patterns are transferred for the construction of semiconductor devices.
The working principle of this process is the removing of part of the resist by exposing it directly to light, in order to get the desired design.
A single iteration of photolithography combines several steps in sequence, as shown in Figure 17.

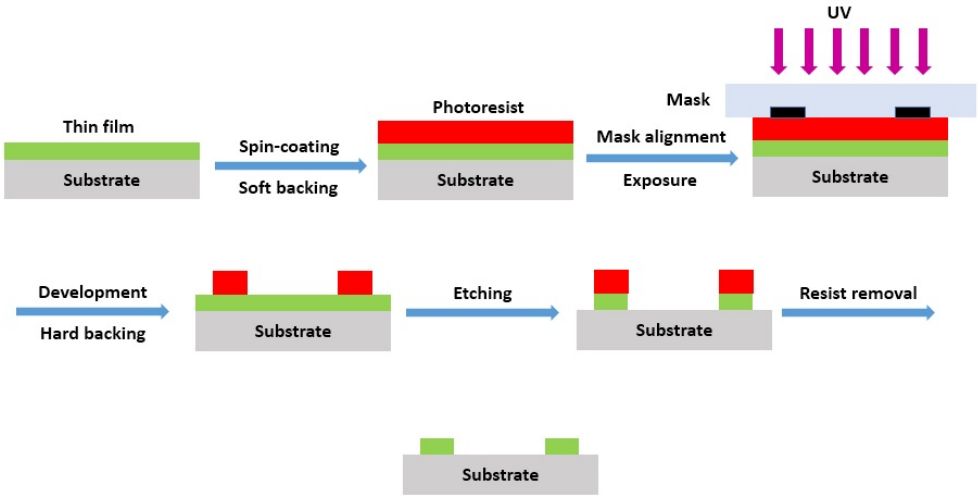

Figure 17: Optical lithography steps [33]

The first step is the wafer surface cleaning in order to eliminate any kind of contamination that could be present. After, there is the wafer preparation step during which the wafer is heated in order to drive off the adsorbed water followed by the deposition of an adhesion layer (primer) used to improve the stability of the resist on the wafer. At this point, the photoresist layer can be deposited in liquid form on the wafer through a spin coating process and then it is evaporated on order to solidify. The final thickness of the deposited resist depends on several factors, as the viscosity of the resist ν and the angular spinning velocity ω, as shown in the equation 48.

$$t = K \cdot S \left(\frac{\nu}{\omega^2 \cdot R^2} \right)^{\frac{1}{3}} \tag{48}$$

A soft bake step is performed to drive off the excess of photoresist. This step is also important for improving the adhesion, the unifor-

mity, the etch resistance and the linewidth control; furthermore the light absorbance caresteristic of the photoresist is optimized. At this point, the mask and the wafer are aligned in order to expose the photoresist only where it has to be removed, following the mask design. In particular, the photoresist is a photosensitive organic mixture containing:

- inactive polymer resins providing mechanical properties such as adhesion, chemical reisstance, rigidity, thermal stability, ...
- photoactive compounds (PAC)
- solvent to control the mechanical properties, i.e. the viscosity of the base, keeping it in liquid phase
- surfactans
- dissolution inhibitors, leveling agents, sensitizers, dyes and others

The photoresist performance depends on different properties, such as polarity, resolution, contrast, sensitivy, that have to be analysed in order select the correct resist to be involved into the process.The polarity can be positive or negative depending on the interaction between the polymer chain and the light. In positive resists, photons are able to break the polymer chains making the exposed resist more soluble in the developing solution. For a negative photoresist, on the other hand, light induces cross-linking of the polymer chains making them less soluble in the developing solution.
The resolution is the capability to differentiate close features on the substrate and results to be related to the critical dimention: the higher the critical dimension, the lower the resolution.
Sensitivity is the minimum energy required to obtain a well-defined feature.
Contrast is the difference between exposed and unexposed area.
At this point, the wafer and the mask can be aligned in order to perform the exposure procedure, resulting the crucial step of the entire process. During the photoresist exposure, a light source emits in a certain wavelength range and the light is focused on the aligned mask-substrate complex going to transfer the mask pattern onto the substrate, and so locally changing the polymeric chain structures. There are different exposure sources depending on the exploited resist and thus on the related wavelength involved in the polymer interaction and also depending on the minimum feature sizes (resolution), that are strictly related to the source wavelength. After exposure, a post exposure bake step can be required in order to re-diffuse the photoactive compund, to increase the resolution and improve the thermal stability.
The exposed or unexposed photoresist, depending on its polarity,

is then removed by means of the development. Wafer is put in an aquesous-alkaline solution that dissolves the soluble areas. Finally a hard bake step is required in order to evaporate the solvents present in the photoresist, to improve etch, implantation resistance, adhesion between photoresist and surface and to stabilize the photoresist.
At the end of the process, after the resist has served its role as protective layer, it has to be stripped. Depending on the current process, the material present on the sample and the exploited resist there are several methods that can be used for this purpose, such as plasma etching, molding, electroplating, lift-off, etc [34]. The lithographic process

in this work is performed through two different equipments, due to different resolution requirments.
For lithographic process using standard UV source for the exposure, the Süss MicroTec MA6/BA6 aligner is used. This is a manual UV exposure system characterized by a $500W Hg(Xe)$ lamp source emitting at wavelengths in a narrow band around $365nm$. It can be used for mask alignment and exposure of UV resists.
When, on the other hand, a higher resolution needs to be reached in the lithograpic step, the DUV Stepper Canon FPA-3000 EX4 tool is used, that is capable to expose devices characterized by a linewidth of $(0.25 - 0.35)\mu m$.
A stepper is a particular exposure tool that works in projection configuration, putting the mask between two set of optical lens, as shown in Figure 18b, thus leading to several advantages: the wafer and the mask are no more in contact, a demagnification ranging from 1X to 10X can be reached meaning that features can be larger and a great resolution can be obtained because only a small portion of the mask is imaged. On the other hand, this tool requires long time for exposure of the entire wafer and since needs a high precision stepper motor, it is complex and expensive.
In a stepper each die on the reticle is exposed separately, so the exposure results in a 'step and repeat' method, in which the alignement is performed just once and it is mantained through a high precision system, allowing the exposure of all dies on the wafer. An optical system (Figure 18a) is used for the reduction of the mask dimension onto a wafer, leading to the possibility of creating defect-free masks at large geometies. In a stepper tool only wafers move in order to expose the different dyes, the reticle stays fixed. The overall system scheme can be seen in Figure 18a.

4.2.3 *Dry Etching*

Dry etching is the proces in which unwanted areas of films are removed by means of a reaction with gases to form volatile products.
In order to selectively remove only the desired area, a photoresist is used to protect the wafer part that have to remain. In this process, the

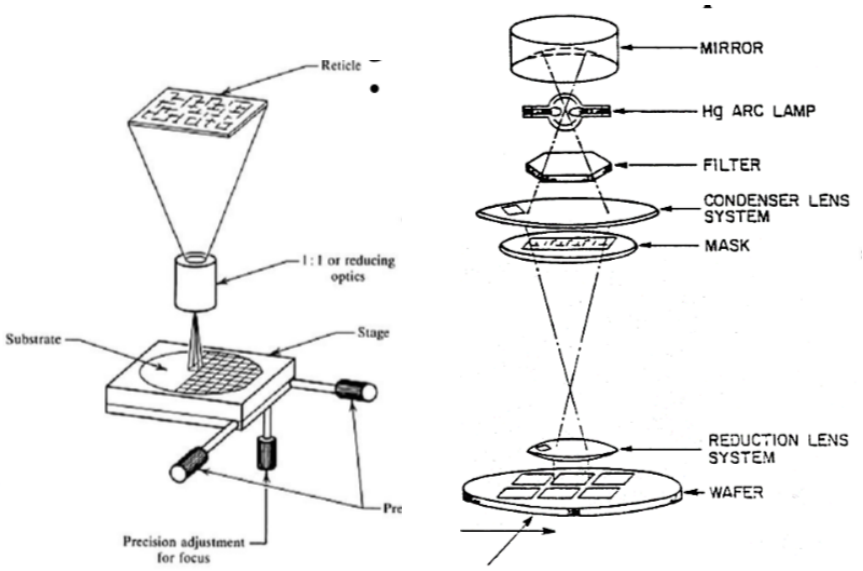

(a) Stepper scheme (b) Optical components

Figure 18: Stepper setup

etch reactants come from a gas or a vapor-phase source. Dry etches can be of two kinds: plasma or non-plasma based. This process shows a lot of advantages with respect to the wet etching one:

- remove the handling of dangerous chemicals
- exploits a smaller amout of chemicals
- both isotropic or anisotropic etched profiles can be obtained
- etching can be directional without using the semiconductor crystal orientation
- can tranfer defined photoresist patterns into underlying layers
- is able to reach higher resolution and cleanliness
- can be better controlled and more versatile

On the other hand, in a dry etching process quite toxic and corrosive gases can be involved, furthermore non-volatile compunds can be re-deposited and this kind of techniques require specialized and so expensive equipment.
The only non-plasma based etching technique is the vapour etching. While there are different plasma-based etching techinques:

- Plasma Etching, using generation of reactive ions or free radicals by electron bombardment at low pressure
- Reactive Ion Etching (RIE) that exploits higher energy ions so leatind to obtain more anisotropic results

- Deep Reactive Ion Etching (DRIE), that instead yields extremely vertical walls.

In this work only plasma-based are used and their working principles are now described.
Plasma is exploited in order to activate reactions at lower temperatures than thermally driven reactions. Furthermore it can provide high directionality of processing and there are several parameters that can be set to obtain the desired properties. Thus, plasma-based etching techniques are able to combine both chemical, so leading to gas reacting with the substrate, and physical, performing a bombardament on the substrate, etching components. Plasma-based dry etching consists of an evacuated chamber that is filled with the gases necessary for the process. Then a RF voltage with a typical frequency of 13.56MHz is applied to a pair of electrodes in order to accelerate free electrons present in the gas increasing their kinetic energy. These electrons collide with the neutral molecules of the gas, ionizing them forming ions and more electrons. After a while, steady state is reached, in which the ionization results to be equal to the recombination (that leads to the visible glow).

There are two types of reactors, the RIE (Reactive Ion Etcher) and the ICP (Inductively Coupled Plasma Reactor).
RIE is a parallel plate capacitive plasma system where the top electrode is grounded and the bottom one is connected to the RF generator that changes the polarity of the bottom electrode. Thus, when polarization is positive electrons are attracted to the RF electrode and ions to the grounded one, while when polarization is inverted, the situation is the opposite. Furthermore, when the alternating voltage frequency is at the radiofrequency range, ions are too heavy to follow it and so only elentrons can reach the electrode. When equilibrium is reached, the bottom electrode will be negatively charged so that a repulsion force lets to not have electrons in the closest region to the electrode. This region is called dark space due to the fact that no collision events occur there and so no excitation and light emission occur. On the other hand, the plasma region results slightly positive leading to an average potential difference with respect to the bottom electrode. Because of that, ions start to be accelerated toward the negative side (dark space) bombarding the sample that is put on the electrode, giving the physical contribution to the etching process. The larger is the potential difference, the higher is the bombardment strength. In a RIE chamber, electrodes are inside the chamber, so the electrons bombardament is directly dependent on the RF power. The limit of this configuration (capacitive coupling) is the corrosion of the electrodes due to the bombardment, strongly dependent on the applied power.
In a ICP chamber on the other hand, a coil is put in the upper part of the chamber. This is made of a non-metallic material so that magnetic

field can penetrate into the chamber. The application of a RF voltage connected to coil, leads to a cyindrically symmetric magnetic field, whose polarity is again dependent on the RF generator. Putting a gas inside the chamber, electrons start to move following the electric field induced by the time-varying magnetic field leading to the formation of a plasma. The difference with respect to the RIE chamber is the fact that there is no presence of electrodes inside the chamber, so no more corrosion problems.

As previously mentioned, several parameters can be controlled in a dry etching process in order to get a specific result, both related to the etchant species generation (gas selection, pressure, excitation power and frequency and electrodes bias) and also to the etchant interaction with the surface (geometrical structure, surface temperature and physical properties of the surface).
An important parameter to evaluate how good is an etching process is the selectivity, defined as the ratio between the etching rates of two different materials. It is strictly related to the gases involved into the process. Taking as example the Si selectivity to SiO_2 and vice versa, the CF_4 plasma is used [35]. The addition of H_2 or O_2 into the chamber can enhance the etch rates of one film over the other:

- addition of small amount of O_2 increases the Si etch rate since oxigen reacts with CF_4 increasing the F concentration
- addition of H_2 decreases the Si etch due to the formation of HF that increases etching og SiO_2

Also the anisotropy is a parameter tightly dependent on the exploited gasses as well as on the applied bias. Indeed adding again H_2 to CF_4 decreases the isotropic etch rate of Si and instead applying a bias will increase the anisotropic etch rate, due to the fact that the ions are directed by the generated electric fied. The two effects can be so combined in order to achieve a very good anisotropic effect for creating quite vertical walls.
To enhance the anisotropy in a etching process, a sidewell passivating process can be added. This consists in the formation of non-volatile products on sidewalls (passivation layer) able to protect the sidewall from incoming radicals, so eliminating the horizontal etch contribution. Practically, conditions can be changed during the process in order to have only polymer deposition. This is done by increasing the C/F ratio that increases the polymerization itself and so the deposition of this passivation layer.
That is actually what happens in a DRIE tool, where very high aspect-ratio walls in silicon can be obtained. In this kind of technique a high-density inductively coupled plasma is achieved and then there is an alternation of etching and protective polymer deposition processes in order to achieve high anisotrpy results with high selectivity.

For the dry etching steps in this work, two different tools are used. The Advanced Deep Reactive Ion Etching (DRIE) Pegasus used for silicon etching steps and the Advanced Oxide Etcher or AOE (STS MESC Multiplex ICP) exploited instead for the silicon nitride etching and for silicon mask openings.

4.3 CHARACTERIZATION TECHNIQUES

In this section a discription of the characterization tools used in this word is developed. In particular, standard optical microscopes (OM) are used in order to check during the process steps the results are the one expected and a scanning electon microscopy (SEM) to analyse more in detail the results obtained during the optimization of the fabrication processes.

4.3.1 *Optical microscopy*

Optical microscopy is a characterization technique that exploits visible light transmitted or reflected from a sample using optical lenses in order to get a magnification of the object. This technique uses photons both as source to excitate the sample and as signal to detect, but it can have different configurations depending on both the sample and the desired results:

- bright-field illumination, in which the contrast of the image is due to the absorbance of the light in the sample
- dark-field illumination, where instead the contrast is because of the scattered light form the sample
- cross-polarized light illumation, that uses the rotaion of polarized light after interaction with the sample
- phase contrast illumination, that exploits the interference of light coming from different paths.
- confocal, that is a scanning technique using a pinhole in order to avoid the out-of-focus light to reach the detector.
- others.

The main limit of this kind of technique is the resolution. Resolution is defined as the shortest distance between two points on the sample that can be distinguished and in an optical microscope and its main limitaion results to be the diffraction effect, strictly related to the source wavelength. The maximum obtainable resolution through an optical microscope is $\sim 0.5\mu m$, due to the fact that the visible light wavelength is around $500nm$.

4.3.2 *Scanning Electron Microscopy*

Electron microscopy is one the most used characterization techniques, leading to overcome the diffraction problems of the optical microscopy thanks to the fact that electrons have smaller wavelength respect to photons leading to get a higher resolution. Indeed, considering the De Broglie relationship, the electron wavelength can be evaluated as

$$\lambda = \frac{h}{p} = \frac{h}{m_e v} \sim 0.4nm \tag{49}$$

and considering the Rayleigh expression [36] for the evaluation of the resolution

$$\sim 0.61 \frac{\lambda}{\alpha} \tag{50}$$

where d is theaperture diameter and $\alpha \ll 1$ is the aperture angle, giving a final resolution $< 10^{-3}\mu m$.
The primary electron beam is now focused by means of electron lenses, composed of ferromagnetic cylindrical material with embedded a series of coils crossed by electric field. This generates an intensive magnetic field that is able to first collimate the beam in a cyilinder and then to focus it on the sample. The minimum spot size is the main limit of SEM resolution: it cannot be lower than $1nm$. The interaction between the primary electrons impinging and the under test sample can lead to different penetration capability depending on the energy of the incoming electrons and also on the mass density of the sample. From this interaction Auger, secondary and backscattered electrons and x-ray photons can be re-emitted depending on the interaction volume and so analysed. For the analysis performed into this work, secondary electrons and backscattered electrons are of interest.

Secondary electrons (SE) come from the fact that when the primiry beam interacts with a solid state matrix, can trasfer energy to a particular atom inside the sample breaking the bonds of one electron belonging to the atom that is so emitted with a very low energy (since most of the primary electron energy is lost for the bond break).
Backscattered electrsons (BSE) on the other hand are due to elastic scattering of the primary electron when interacting with the sample and for that reason their energy is kept almost constant.
One of the main issues of the electron microscopy is the so-called charge effect. When characterizing non conductive material samples, electron can start to localize on the surface, forming a sort of shield against both the primary beam and both BSE and SE, thus distorting the final image. This problem can be reduced in case of the presence of a thin insulator layer on the silicon wafer and without changing the morphology of the sample, just increasing the accelerating voltage, in order to give to the electrons enough energy to overcome the

layer. The Zeiss Supra 40 VP SEM is used in this work to perform electron microscopy. This tool is characterized by four types of detectors: in-chamber SE, in-lens SE, high definition four quadrant angular selective BSE (HDAsB) and variable pressure SE (VPSE). Moreover, has an acceleration voltage ranging in $20V - 20kV$ and can reach a maximum resolution of $1.3nm$.

4.4 PROCESS FLOW

In this section the descrisption of all the steps involved the whole process flow is done. The overall process flow is tabled in Appendix 8.

4.4.1 *Wafer preparation*

The fabrication starts with a $350\mu m$ thick, 4", double side polished silicon wafer where a uniform SRN layer is deposited through a LPCVD process. A $320\mu m$ thick layer of SRN is uniformaly deposited on the wafer through the LPCVD nitride furnace. To achieve this goal, 1 hour of deposition is required being the deposition rate around $5.3nm/min - 5.4nm/min$ at a working temperature of $810°C - 850°C$, in enviroment kept at a pressure equal to $150mTorr$ and using as process gasses $SiH_2H_2Cl_2$ and NH_3 with a gas rate of 80 sccm and 50 sccm, respectively.

4.4.2 *DUV front side patterning*

The heat and mass sensitivity of a hollow MEMS sensor are both dependent on the SRN cross-section. In particular, the area needs to be minimized in order to reduce the resonator mass and thus to increase the mass sensitivity. Moreover, also the flux of heat into the silicon substrate is lowered, increasing in this way the heat responsivity. In this process, the wall thikness is established by the second LPCVD step for closing the channel surface and, in particular, it results to be dependent on the openings width in the SRN mask layer. As already explained in the original work [16], the optimized dimensions of the openings are $0.9\mu m$ x $1\mu m$ separated by a $1\mu m$ gap, resulting too small to ensure a perfect pattern transfer using a standard UV lithography process due to the resolution limitations of this technology ($\sim 1.25\mu m$). For that reason, the deep UV lithography technology is exploited, being it characterized by a resolution lower than $250nm$ [37].

The entire channel shape is given by the union of two specular half channels joined together to get a unique continous channel.
In order to get the varying channel shape, the DUV design si modi-

fied in such a way that the two halves are separated by a certain gap, whose exact dimension is chosen with respect to the results obtained in section 6.1. Thus, before building the definitive channel, a 6x6 matrix of different channels characterized by an increasing gap going form 0µm to 35µm with a step of 1µm is made.

The deep ultra violet lithography step starts spinning a DUV resist consisting of 60nm BARC layer (Bottom Anti Reflection Coating) soft baked for 60s at 175°C and a 750nm layer (JSR-M35G) soft baked for 90s at 130°C, by using the Süss MicroTec Gamma 2M spin coater. An exposure dose of $250J/m^2$ is used in the Stepper tool and finally the development is performed in a single puddle TMAH Stepper developer for 60s after a post-exposure bake of 60s at 130°C.

The pattern is then transferred from the resist to the frony SRN layer through 2 dry etches processes in the AOE tool. First, the BARC layer needs to be etched as anisotropically and selectively as possible. For this aim the *barcetch* recipe is used, whose parameters are shown in table 3, with an etching time of 90s.

Table 3: AOE barcetch recipe process parameters

BARCETCH process		
Process gases	CF_4	H_2
Flow rates (sccm)	4	20
Pressure (mTorr)	1	
Coil power (W)	400	
Platen power (W)	100	
Process temperature (C)	0	

After, the SRN layer is anisotropically etched in the same tool for 6 minutes and 30 seconds using the standart SiO2_RES recipe, described in table 4.

Table 4: AOE SIO2_RES recipe process parameters

SIO2_RES process			
Process gases	C_4F_8	H_2	He_2
Flow rates (sccm)	4	20	174
Pressure (mTorr)	4		
Coil power (W)	1300		
Platen power (W)	200		
Process temperature (C)	0		

In fig. 19a the final result of this etch step can be seen, while in fig. 19b the presence of the gap is underlined.

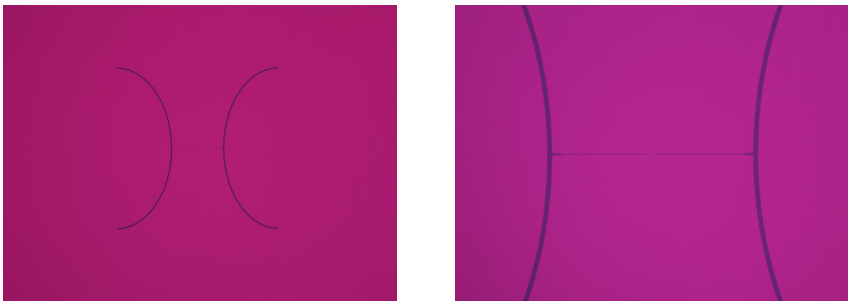

(a) Front side DUV patter (b) Zoomed front side DUV pattern

Figure 19: Optical microscope picture of the SRN etch

Before moving on with the pattern of back side fluidic inlets, the resist is stripped through a standard oxygen plasma cleaning and a PECVD silicon nitride protective layer 640µm is deposited on the front side through the PECVD system. The exploited recipe is the standard *LF SiN*, whose paramenters are summarized in table 5.

Table 5: PECVD4 LF SiN recipe process parameters

LF SiN process			
Process gases	SiH_4	NH_3	N_2
Flow rates (sccm)	30	15	1470
Pressure (mTorr)	550		
Coil power (W)	60 LF		
Deposition rate (nm/s)	55		
Deposition time (min)	16		

4.4.3 *Fluidic access channels*

A standard UV lithography step is performed on the backside of the wafer in order to pattern the fluidic access holes.
Before the resist spinning, the wafer surface is treated with HMDS for hydrophonicity, then a 2µm thick layer of negative nLoF 2020 resist is spinned on it and finally a soft baking process at 110°C is done. In this case, the exposure is performed by the MA6/BA6 aligner, where a backside alignement is performed: the mask alignement marks are found and their image is grabbed to be aligned with the alignment marks placed on the top side of the wafer. The exposure is performed with a dose of 65 mJ/cm^2 in close proximity configuration, with a

gap of 10µm between the mask and the wafer in order to not to be too close to stick the resist on the wafer.
After a 60s PEB at 110°C and, in the end, a single puddle TMAH development are run.

Before etching through the whole silicon wafer in order to connect the access holes with the front side channel, an anisotropic SRN etching step is performed, using again the SIO_RES recipe in the AOE tool (tab. 4), now for 150s being the hole dimensions higher and so leading to an increased etch rate.
At this point, a two step Bosch process (*Process A* recipe) is used in the DRIE Pegasus tool, whose parameters are shown in table 6.

Table 6: DRIE Pegasus Process A recipe process parameters

Process A						
	First step			Second step		
	Etch		Dep	Etch		Dep
	start	end		start	end	
Process gas	SF_6	SF_6	C_4F_8	SF_6	SF_6	C_4F_8
Gas flow (sccm)	350	550	200	530	550	200
Cycle time (s)	1.5	5.5	4	1.5	5.5	4
Pressure (mTorr)	25	90:150	25	150	25	
Coil power (W)	2800	2800	2000	2800	2800	2000
Platen power (W)	120:140	45	0	140	45	0

The resist is thus removed in the same way as in the end step of section 4.4.2. Before coming back to work on the front side, the protective nitride layer must be removed. A burried HF solution is used for isotropically etching the deposited layer. From the process specification the etch rate results to be variable and around 10nm/min, so in order to ensure that all the nitride is removed the process is performed for 65 minutes.

4.4.4 *Surface channel shaping*

At this point the wafer is washed for a time >15min in order to shape the channel through an isotropic silicon etch process using the DUV patterned SRN as mask layer.
The recipe exploited is the *mediumiso* one, whose parameters are shown in table 7. The etch rate depends on several parameters and can be

Table 7: DRIE Pegasus mediumiso recipe process parameters

MEDIUM ISO process	
Process gases	SF_6
Flow rates (sccm)	150
Pressure (mTorr)	25
Coil power (W)	600
Platen power (W)	3
Process temperature (C)	20

highly variable during the same process. In order to have an idea of the final result, figure 20 can be observed. In this step, the SRN film,

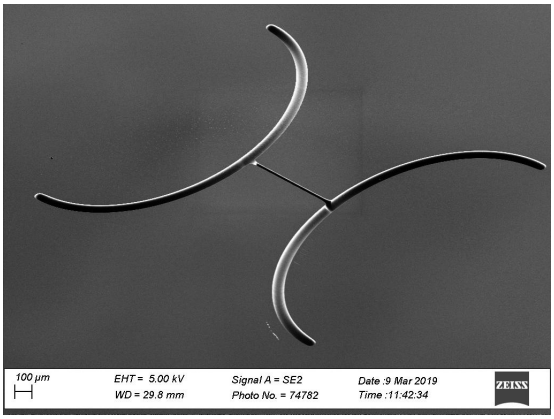

Figure 20: SEM images of the channel shape after 30 minutes of DRIE etching with a tilted angle of 50°. To get the image through the SEM tool, the SRN layer has been removed solving in this way the charge effect issue.

previously DUV patterned (see section 4.4.2), is used as etch mask.

4.4.5 *Channel closing*

At this point the channel needs to be closed by means of deposition of a SRN layer. Before doing this, the sample has to be cleaned in order to remove any residual of previous processes. To this aim, a RCA cleaning is performed.
A LPCVD SRN deposition process is then performed in the same way as the described in section 4.4.1. In this case a deposition time of 1 h and 42 min is done giving a final deposition thickness of around 540nm, in order to ensure a proper sealing of the channel. The result after this deposition is shown in figures 21

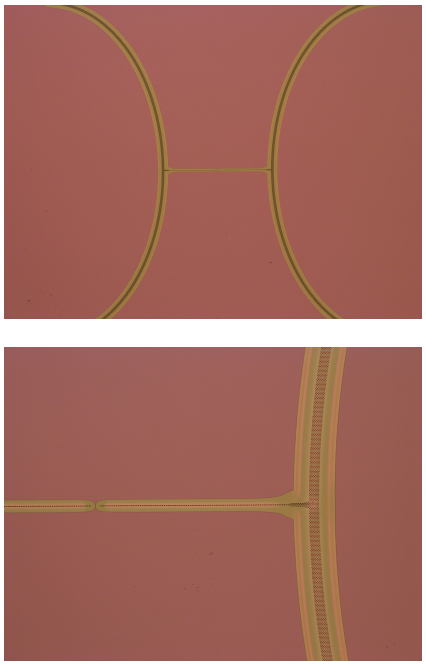

Figure 21: OM images of the front side of the channel after deposition of a SRN closing layer

4.4.6 *Resonator release*

The final step of the process is the channel release. To get this aim, first the SRN layer, now thick around 1µm, has to be etched. So another lithograpic process is perfomed: the wafer is treated with HDMS, then 1.5µm of AZ 701 MR resist is deposited and after a soft baking process at 90° for 60s is done.
The substrate is then aligned to the mask and the exposure is performed, in hard contact configuration with an exposure dose of $160 mJ/cm^2$. After exposure, a 60s proximity PEB at deg 110C an 60s of single puddle TMAH development are performed.
To perfom the release, trenches 11µm in width and 500µm in length around the resonator channel are opened.

For etching the SRN layer, 10 minutes of SiO2_RES (table 4) process in the AOE is run, the resist is thus removed through a standard plasma ashing process and finally, in order to isotropically etch the silicon around the resonator channel a *mediumiso* (table 7) process in the DRIE Pegasus is run for 10 minutes. The final results after the resonator release are shown in figures 22a and 22b. In particular, the SEM image shows the cut of the released channel in the central point and from the picture it can be seen how this central point of the channel results to be characterized by a very well defined narrower circle. A small disalignment can be noticed between the channel and over closing SRN layer. This is due to the fact that in the last lithography step, the mask was designed in order to align the marks present on it

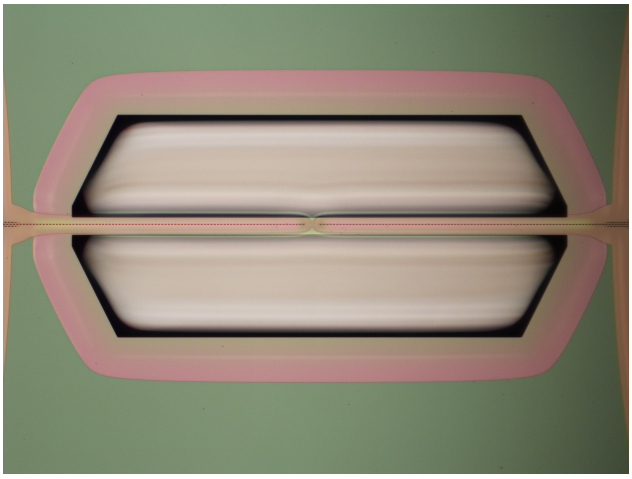

(a) OM image of the top view of the released hollow resonator

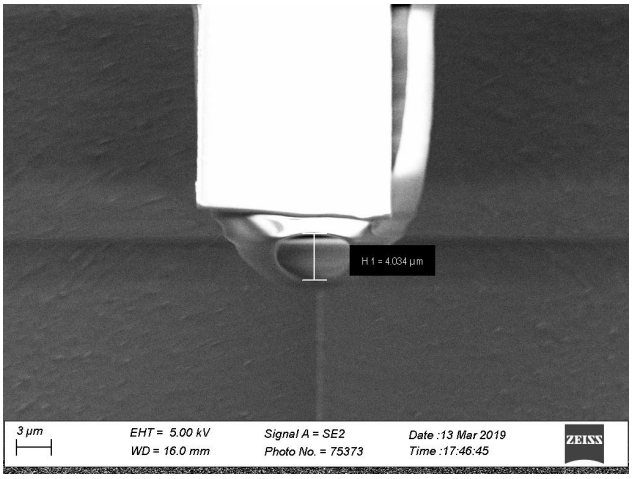

(b) SEM image of the cross section of the channel in the central point of the released resonator

Figure 22: Released resonator

with the metal electrodes pattern that in this work is skipped. For that reason, the alignment is performed directly on the resonators and it results to be a very tricky step.

5 EXPERIMENTS

In this chapter, first a brief description of the experimental equipment involved is presented and then the protocol of the experiments performed for the frequency characterization of the developed device is described.

5.1 LABORATORY EQUIPMENT

An overview of the equipment exploited is here presented, together with a brief description of its working principles.

5.1.1 *Laser Doppler Vibrometer*

A laser Doppler vibrometer (LDV) is an instrument exploited for performing non-contact vibration measurements of a sample.
This tool is generally made of a two beam laser interferometer measuring the frequency or phase difference between a reference and a test beam. Several laser sources can be used to excite the target, then scattered light from it is collected together with the reference beam on a photodetector.
As can be seen from the schematic representation of the vibromiter (fig. 23), the beam coming form the laser with a starting frequency f_0 is splitted into reference and test beam by a beam splitter. Thus, the test beam goes through the Bragg cell, an acousto-optic modulator used for giving to the beam a certain frequency shift f_b [38]. The shifted test beam is so directed towards the target, that because of its vibration gives to the beam a Doppler shift equal to

$$f_d = 2v(t)\frac{\cos\alpha}{\lambda} \tag{51}$$

where $v(t)$ is the target velocity, α is the angle between the laser beam and the velocity vector and λ is the wavelength of the beam. Due to the interaction with the target, light scatters in all direction and a small part of it can be so collected again by the vibromiter being thus reflected towards the photodetector. The final frequency of the beam is then:

$$f = f_0 + f_b + f_d. \tag{52}$$

This scattered light combines with the reference one at the photodetector. So the basis principle of an laser doppler interferometer is the optical interference between two coherent light beams, for which the

relative light intensities are required to overlap. The final intensity due to interference of the two beams is modulated according to

$$I_{tot} = I_1 + I_2 + 2\sqrt{I_1 I_2}\cos\left(2\pi\frac{r_1 - r_2}{\lambda}\right) \tag{53}$$

where the last is the interference term that relates the difference of the two path lenghts of the two beams.

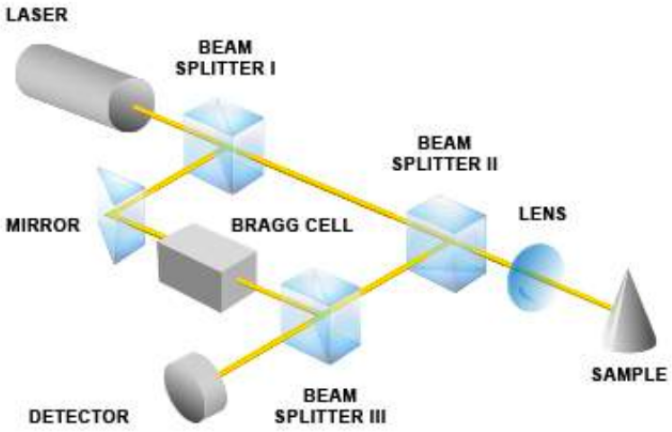

Figure 23: Scheme of the Laser Droppler Vibrometer from Polytec website

5.1.2 *Micro System Analyser*

In this work a microscope based reference laser-Doppler vibrometer by Politec GmbH (MSA-500) is used (figure 24). This is used for non-destructive and non-contact measurements of three-dimensional movements in mycrosystems. This tool measures out-of-plane movements using the Microscope Scanning Vibrometer (MSV) based on laser interferometry and in-plane movements through the Planar Motion Analyzer (PMA) based on video microscopy, stroboscopy and digital image proessing [39].
The system is made of different components:

- the sensor head containg the interferometer connected to the measurement microscope by a fiber
- the controller, whose aim is to decode the intereferometer signal coming from the sensor head using a velocity decoder
- the Data Management System, used for recording the measurement data.
- a PC in order to generate and synchronize the control signals
- the junction box for connecting the MSA components and for providing interfaces for peripheral devices

Figure 24: Laser-Doppler vibrometer MSA-500 by Politec GmbH

- a measurement microscope, where stroboscopic light is generated for PMA measurements allowing for video microscopy and digital image processing for in-plane movements. Moreover, piezo scanners are present in order to deflect the laser beam for MSV measurements.

5.1.3 *Phase Locked Loop*

The PLL is a control system that produces a reference signal whose phase is related to the one of the input signal, allowing to measure the shift of frequency in an excited resonating structure [40]. In particular, there is a phase delay between the drive signal generated by the PLL and the system response and as a result of an external perturbation, a delay between the drive and the response can be induced. The PLL is designed in order to adjust the frequency of the drive signal in such a way to restore the required phase delay.
A PLL is made of three main parts designed in a feedback configuration. A phase detector compares the phases of the input signal and the reference one coming from the oscillator. The difference needs to be equal to the phase set point and if it deviates from that value, an error signal is generated that has to be minimized. To this aim there are the PI controller and the oscillator: if the error is positive, the reference signal is delayed with respect the input signal, so the oscillator frequency has to be increased, if the error is negative, on the other hand, the oscillator frequency has to be lowered.
Thus, the purpose of a PLL system is to track in a accurate way the

frequency changes of a resonating system.
In this work, the input signal is the output of the vibrometer and the reference one is generated internally by the equipment. These two signals are then compared in their phases and sent to the PI component that controls a voltage controlled oscilloscope in order to obtain an output with the same frequency of the input. The block diagram of the PLL system is shown in figure 25.

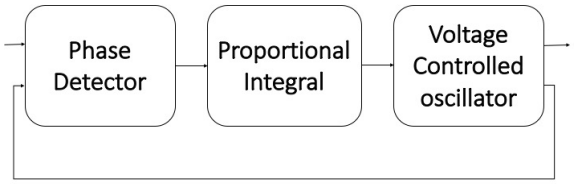

Figure 25: Block diagram of the PLL

An importan figure of merit of PLL system is its bandwidth, defined as the maximum rate at which the PLL can restore the correct phase delay. Its value influences the PI gain and the time response of the detection. Working at low bandwidth leads to get better quality of the registered signal (high SNR) but with a higher integration time, while a high bandwidth allows to obtain faster performances but with a lower quality (lower SNR).

5.1.4 *Vacum chamber and pumps*

In order to provide vacuum into the chamber, a set of two pumps is exploited. A rough pump from Leybold AG coupled with a turbo pump from Pfeiffer Vacuum (figure 26) allows to reach a high vacuum conditions with a pressure value of 10^{-5} mbar.

5.1.5 *Setup*

The chip is cut from the wafer by means of a diamond pen so as to be put into the vacuum chamber on the top of a piezoelectric crystal that has to be provided of the signal generated by the PLL system. The chamber is thus positioned under the LDV system and centered in order to have the emitted laser pointed exactly on the resonator present in the chip. The important issue in this setup is the correct position, in terms of inclination, of the chip on the piezoelectric support. Indeed, the chip must be perfectly perpendicular to the direction of the laser beam, that comes from the top, in order to have the maximum reflected light possible arriving on the LDV system. In this way,

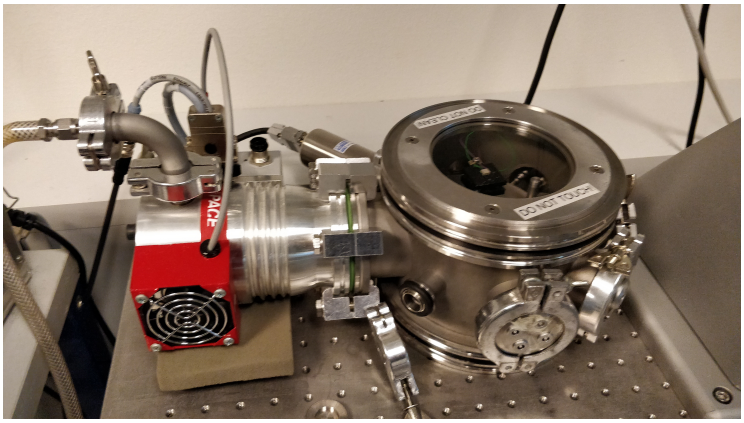

(a)

(b)

Figure 26: Vacuum pump system

the behaviour of the excited resonator is measured and the resulting measurements are analyzed by the PLL, whose aim is to take information about the frequency shift of the system. The final setup of the chip into the vacuum chamber is shown in figure 27.

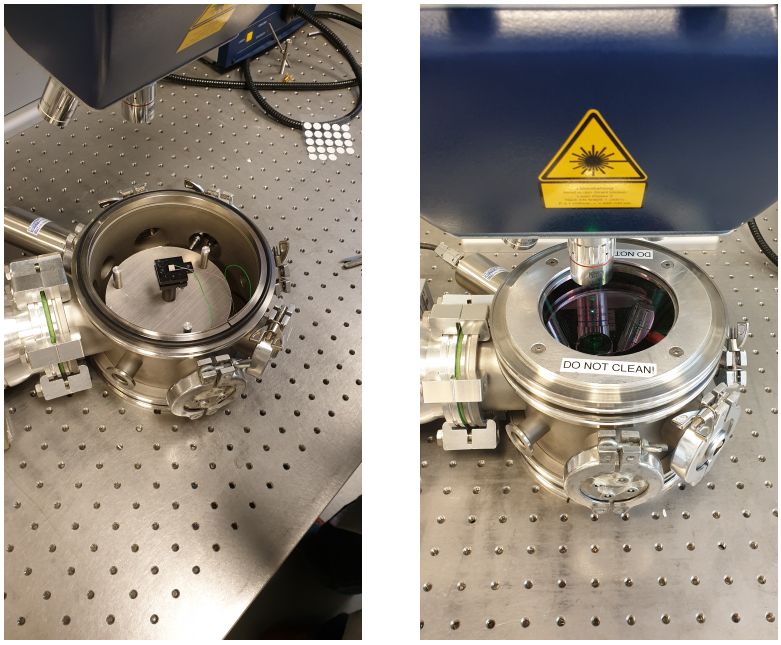

(a) Positioned piezoelectric crystal on the support inside the chamber

(b) Closed chamber with the alignemnt of the chip positioned on the piezocrystal iwth the laser of the LDV system

Figure 27: Final setup of the chip inside the vacuum chamber

5.2 MEASUREMENTS

In order to have a good characterization of the developed structure, the same protocol is performed for different final chips. The device is placed into the vacuum chamber on top of the piezocrystal, paying attention to not be tilted. At this point, the covering glass is put in order to seal the chamber and the pumps are turned on to get the vacuum ($10^{-}5mbar$). The laser of the vibrometer is turned on in order to center the system under test, positioning the beam in the central point of the structure. At this point the PLL is configurated:
the input range is put to 2.1V to be sure to not go over range with the signal, the differential signal is turned off and the AC is activated, meaning that the DC part is take away and the sampling rate is set. About this, working with aroung 500Hz means that at least 3600 samples per seconds are necessary. After, since one frequency only has to be actuated, the output signal amplitude is set to $10mV$.

Once all the parameters are set, a frequency sweep is made with the piezocrystal in order to find the exact resonance frequency, sampling in a certain frequency range with around 100 points in order to get the exact value of the frequency and phase. Automatically, also the relative quality factor of the structure is taken from the sweep measurement.

Starting from these obtained values, they are now inserted into the PLL settings as central frequency and phase set points. The bandwidth of the PLL is thus set to a value in a range between 500Hz – 1kHz in order to minimize the error, as explained in section 5.1.3. Now the measurements can start, checking that the error of the phase stays around the 0. At this point, the frequency data elaborated over time from this measurement can be saved for around 10 *minutes* in order to be used for the evaluation of the Allan Deviation of the current SMR.

Part IV

RESULTS AND DISCUSSION

6 RESULTS

In this chapter there is an overview of the results obtained during this project. In the first part, a description of the optimization results achieved during the fabrication is presented, while in the second part of the chapter the frequency and Allan Deviation characterizations of the final resonator structure are shown.

6.1 FABRICATION OPTIMIZATION

Regarding the fabrication process, two steps are mainly investigated in order to obtain the desired resonator. In particular, the backside inlets and the channel dimensions and shapes need to be designed in such a way to face the requirements previously explained in section 1.3.

6.1.1 *Backside Inlets*

For the backside inlets, two different dimensions are considered. In particular, this step is a photolithography step (see section **??**), but now a Maskless Aligner tool is used, allowing to directly draw the shape of the pattern to be processed without any kind of mask, so reducing the cost of the process and obviously making it easier from an optimization point of view.

The backside inlets are simple circles, characterized in this case by a diamenter of 50µm and 100µm that are patterned on the wafer in order then to perform an anisotropic etch step (Process A describe in tab. 6) in order to etch through the entire silicon wafer.
The issue of this step is to find the exact number of cycles of the second step of the etching process necessary to etch through the whole silicon. This results crucial since the inlets from the back side of the wafer need to reach the front side in order to ensure the flow of the fluid inside the channel. On the other hand, the number of cycles cannot be too high, just to be sure to reach the previous aim, since keeping etching can be dangerous both for the machine and for the wafer due to the realease of gases from the back of the wafer.
In the end, the number of cycles has to be the ones for which the final etched profile results to be as the one shown in figure 28.

In order to know the exact number of cycles of the second step of the process are necessary for the two different cases a new recipe involving only the second step of the process is created. The number of

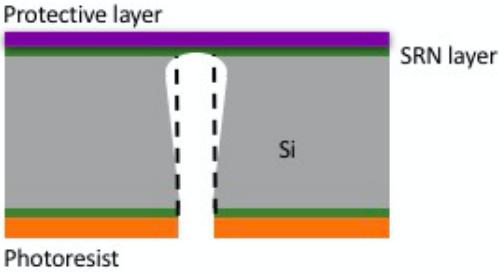

Figure 28: Cross section sketch of the wafer after the etching process of the backside fluidic access.

cycles of the first step is always fixed to 11, while the second step ones need to be differently tuned. In particular, the etch rate is dependent on the size of the hole, so it cannot be assumed to be constant and thus different attempts are performed starting from a fixed number of cycles of 50. In order to add to this starting value only cycles of the second step, an on-purpose recipe is created, in which the first step is removed.
One finds that in order to etch though the bulk of the wafer with a hole diameter of 50μm, 124 cycles are necessary showing an average silicon etching rate of 14$\mu m/min$.
The same process is performed using backside holes diameter equal to 100μm. In this case, the number of cycles necessary for obtaining the same result is 98, showing in this case an predictable increased average etch rate equal to 17.5$\mu m/min$.

As expected the etch rate increases with the increase of the hole dimension even if there are two different competitive effects. On one hand, the transport of reactive products is made easier in these high aspect ratio holes by increasing their diameter, thus resulting in an increase of the etch rate; on the other hand, the increased etched area (4 times larger) dilutes the availability of reactive agents in the etched holes and so the etch rate goes down due to larger loeading. Overall, the load is $<<$ 1% so the effect of increased etch rate is larger. Furthermore, the evaluated rates are average values, so they cannot be considered as a constant rate during all the process. ,

6.1.2 *Channel shape*

Starting from the array of chips previously patterned (see section 4.4.2), each characterized by different gap between the two halves of the channel, this section is divided into two steps in order to understand which is, first, the optimal etching time for the desired channel dimensions and then the right gap between the left and right halves.

Thus, the same etching process is performed for all the chips with different etching times, in order to compare the final etched profile and select the most suitable ones. In particular, the typical channel profile that comes out from this process results to be a nearly cylindrical shape, characterized by a certain radius and an etched depth $\sim \frac{4}{3}r$.
The implemented etching times with the corresponding results are shown in table 8. In order to take the reported measuements, SEM characterization is used. In particular, to get the etched width a simple front side imaging is enough, as shown in fig 29, while for the etched depth evaluation the measure is performed by tilting the sample at an angle equal to 15° and so using a simple trigonometry equation (eq. 54) to get the real depth (fig. 30).

$$\text{real depth} = \frac{\text{measured depth}}{\sin 15°} \tag{54}$$

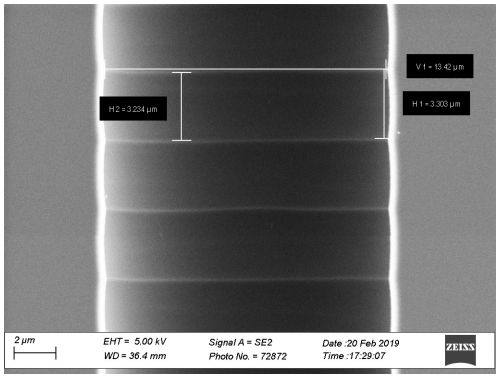

Figure 29: SEM image of the front side of the channel for measuring the etched width after 15 min of isotropic Si etching.

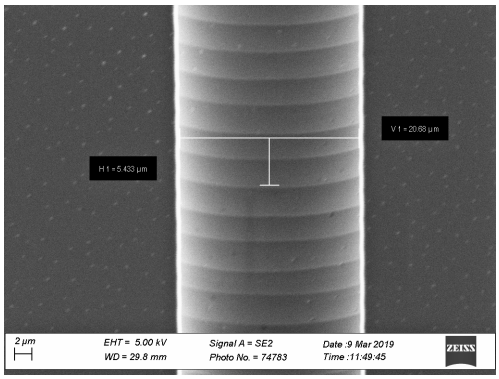

Figure 30: SEM image of the channel with a 15° tilted sample for measuring the etched depth after 30 minutes of isotropic Si etching.

Regarding the etched volume instead, several tricks are taken: the volume of cylinder cut along the plan parallel to the long side is

evaluated as the difference of the entire cylinder minus the one of the cylinder segment, as shown in fig. 33.

Table 8: Channel Etch results at different process time.

Etching time (min)	10	12	15	20	25	30
Etched width (μm)	10.9	11.9	13.4	15.8	18.7	20.9
Etched depth (μm)	10.3	11.7	12.7	16.4	19.1	21.1
Etched volume (μm^3)	598.3	813.7	925.7	1582.2	2185.3	2602.3

From the previous results the width, the depth and volume etch rates are evaluated by simply dividing them for the relative etch times and their trends are plotted in figures 31, 32 and 33.

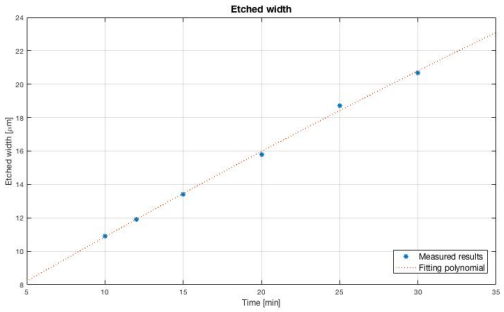

Figure 31: Plot of the lateral etch results.

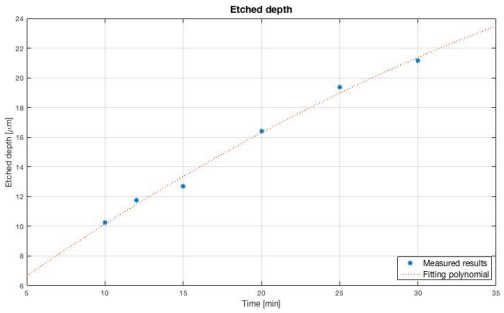

Figure 32: Plot of the depth etch results.

Intrestesting considerations can be extracted plotting the rates of each of this etched profile, as it can be seen in figure 34. From the plot it is clear how there are two different competitive mechanisms in the etch rate trend. In detail, at the beginning there is only a little bit exposed surface, so the etch starts at full force both in depth and in lateral direction (so also for the volume that is directly dependent on time), the initial rates resutl more or less linearly incresing, meaning that at the beginning the process is fundamentally limited by the fact that the surface to be etched is growing and thus by the availability

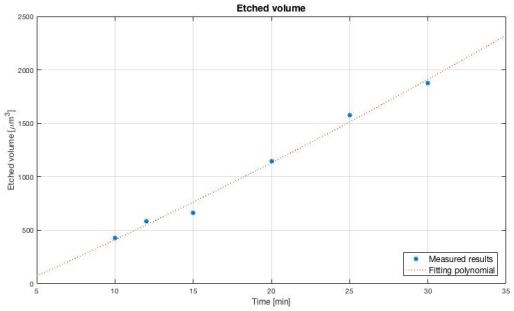

Figure 33: Plot of the volume etch results.

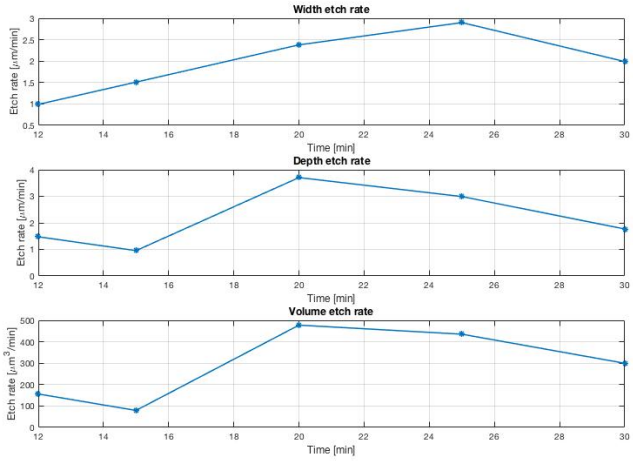

Figure 34: Trend of the measured rates for depth, width and volume etches

of the reactive gas, that in time is constat, with respect to the exposed area, that in time is rising, so they result diluted more and more.
But going on, and looking in the specific at the last point of the data of the volume etch rate (figure 34, it indicates that the volume etch rate is decreasing at that point, meaning that it is limited by the diffusion of the reaction products out of the cavity underneath the SRN layer. What should comes out having more result, should be a saturation of the etch rate representing the compensation of the two competitive contributions.

Analyzing the obtained channel dimensions, the optimal one results the one coming from 25 minutes of etching, whose depth is $\sim 19\mu m$. In this way, indeed, the immuno-cell flow into the channel is allowed, without increasing too much the SCR dimension and so without lowering the peformance of the resonator.

At this point, the dimension of the channel in its central point has to be tuned. To reach this aim, all the structures coming from the 25 min etching are considered. Being the immuno-cell diameter on average equal to $\sim 14\mu m$, the central hole needs to be around $10\mu m$ in order to ensure the cell to be arrested in that point.
By means of the SEM supra 3 tool, the different structures are analyzed. The measurements are taken by tilting the sample of 60° in order to get a measure as close as possible to real one. As it can be seen from the graph in fig. 35, the optimal design results to be the one characterized by a gap equal to $14\mu m$, for which the diameter of the hole is about $10\mu m$. In figure 36 the shape of the central hole and its releative dimensions can be observed. Again to get the real vertical dimension of the hole, equation 54 is used.

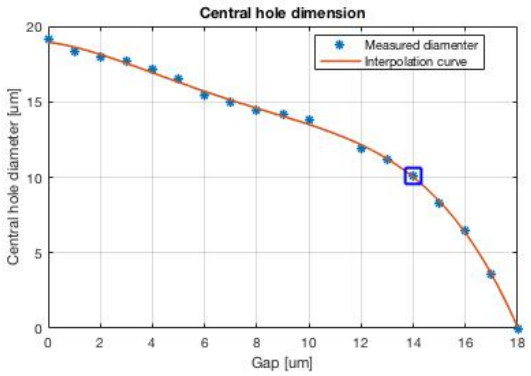

Figure 35: Plot of the central hole diameter versus the gap between left and right halves of the channel after 25 minutes of insotropic Si etch.

The final resulting channel shape, selecting 25 minutes of isotroping silicon etching for a structure characterized by a gap equal to $14\mu m$ can be found in figure 37. Also in this case, the image is taken by tilking the sample with an angle of 60°, in order to visualize the presence of the hole in the center of the channel.

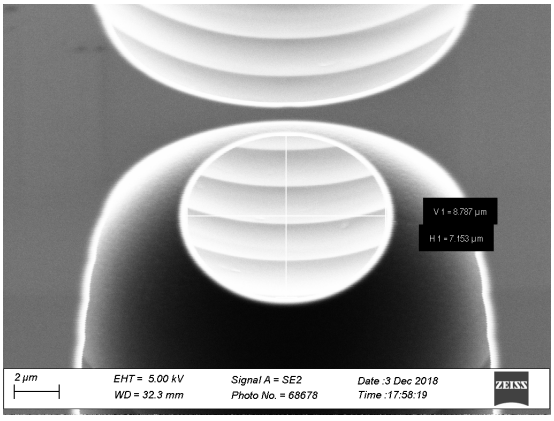

Figure 36: SEM image of the central hole for 14µm gap structure.

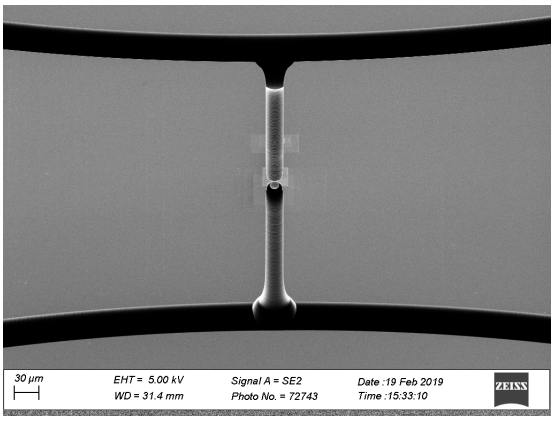

Figure 37: SEM image of the final channel shape after 25 minutes of isotropic etching with a gap between the two halves equal to 14µm.

6.2 FREQUENCY CHARACTERIZATION

In this section, the obtained SRNs are characterized in their frequency behaviour and stability. To do that, the protocol explained in section 5.2 is followed. In particular, two kind of chips are used: four characterized by a higher realeased area - that are the central chips in the entire wafer- and five with a lower released volme.

6.2.1 *Resonance frequency and Quality factor*

As previously explained, the starting point is the measurement of the refonance frequency of the structures under test by means of the sweeper, in order to detect the vibrational response for extracting the resonance behaviour, i.e. resonance frequency and quality factor.
From the obtained data, it is possible to build the amplitude and phase plots, whose shapes are shown in figures 38 , 39 in which the curves are obtained by fitting the experimental data with a quasi-Laurentian function, showing a very well fit.
As it can be seen from the previous plots, the peaks result well

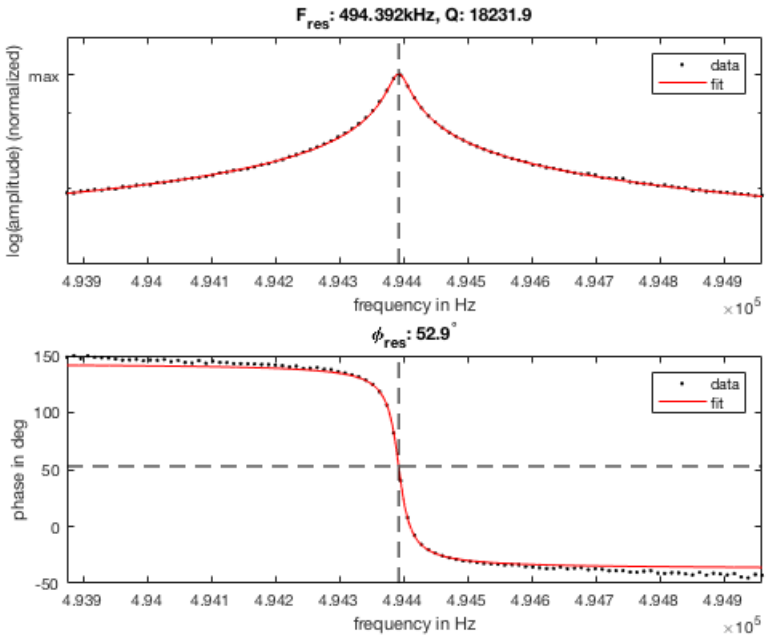

Figure 38: Plot of the amplitude and phase trends around the resonance frequency of the structure with lower released volume coming from the sweep measurement

shaped for both the structures and also the trend of the phase is characterized by a nearly perfect flat trend far from the resonance frequency and by a very steep transition around it, showing a very high slope. Furthermore, the symmetry of the phase and amplitude signal shows that the resonator is operating in the linear regime, where

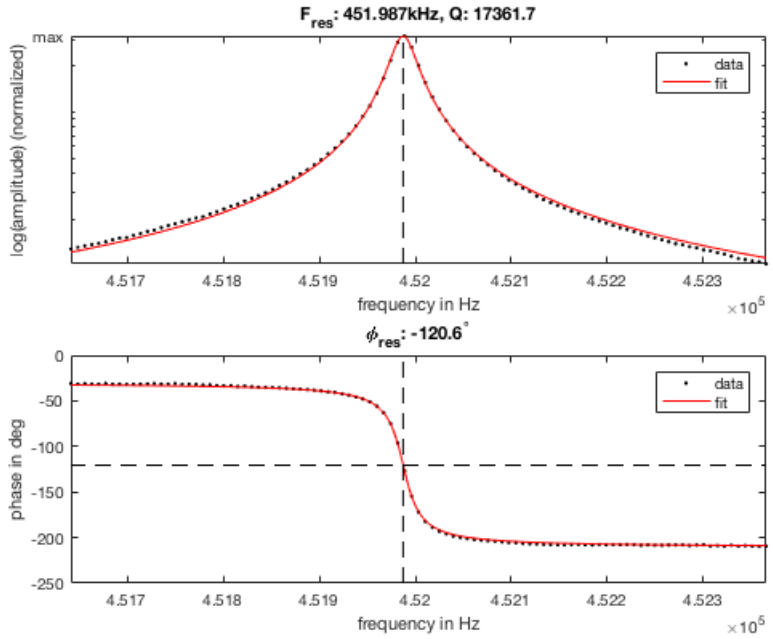

Figure 39: Plot of the amplitude and phase trends around the resonance frequency of the structure with higher released volume coming from the sweep measurement

the equations explained in the theoretical discussion make sense. The results are confirmed also by the other structures, presenting a resonance frequency around 495 kHz for the lower released volume resonators and around 455 kHz for the higher released volume ones. This result confirms that the fabricated resonators are fully released, withouth any connection with the substrate. The resonance frequencies with the corresponding quality factors are tabulated in tables 9, 10.

The Q factors result quite variable, even if for the most of the tested structures it is found to be consinstent with the order of magnitude resported in literature ($\sim 10^3 - 10^4$) [41], [42], [43]. Considering that a typical quality factor for a resonator submersed in a liquid is around $\sim 2 - 50$, this confirms how good are the obtained results in terms of quality factor - from these measurements it results higher of at least 2 order of magnitude.

Table 9: Resonance frequencies and quality factor of the four SMRs with higher realeased area

SMR	1	2	3	4
f_{res}(kHz)	452	455	455	462
Q_f	17362	8004	1947	10271

Table 10: Resonance frequencies and quality factor of the four SMRs with lower realeased area

SMR	1	2	3	4	5
f_{res} (kHz)	494	493	494	492	497
Q_f	9133	9118	18232	13571	16643

6.2.2 *Allan Deviation*

In order to characterize the resonator MEMS in its frequency stability, the Allan Deviation of the SCR is measured, tracking, as already explained, the resonance frequency through the PLL.
Data are acquired for about 10 minutes and then, a matlab script is used in order to obtain the AD plot, whose typical obtained trend is plotted in figure 40.

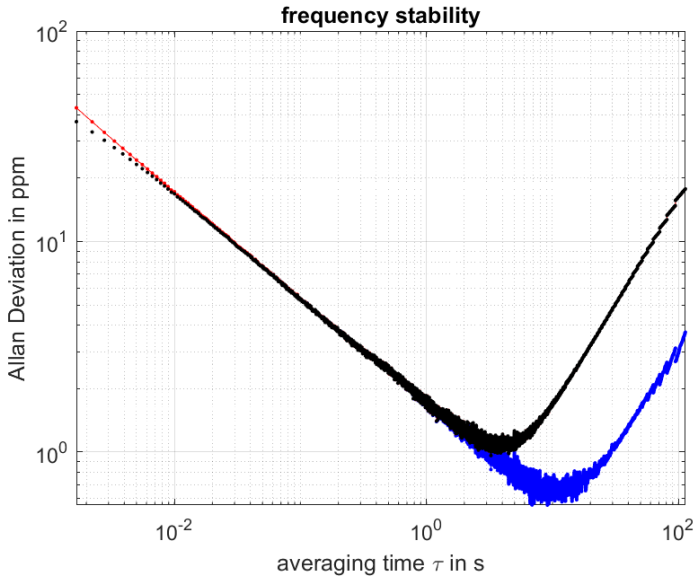

Figure 40: Plot of the Allan Deviation versus integration time in logarithmic scale obtained for the SMR with a higher released volume

In the previous figure, two different plots are present. The blue one is traslated in the right part of the graph towards lower values, this is because in the blue line the linear drift is removed. The trend seems to consinstent with the theoretical one, but in order to validate it, the left and right slopes have to be evaluated by fitting the curves. To do this, since the extracted data are presented in an exponential scale, first all results are logarithmically tranformend in order to treat them with polynomials. Thus a first order polynomial fitting is exploited, obtaining the coefficients m and q of the following line equation:

$$y = mx + q \tag{55}$$

where x is the integration time, y the Allan Deviation, m, represents the slope of the line so giving information about the origin of the noise and q tells how big the noise component is for that resonator. This is done for all the analysed resonators, obtaining the results showed in figures 41, 42.

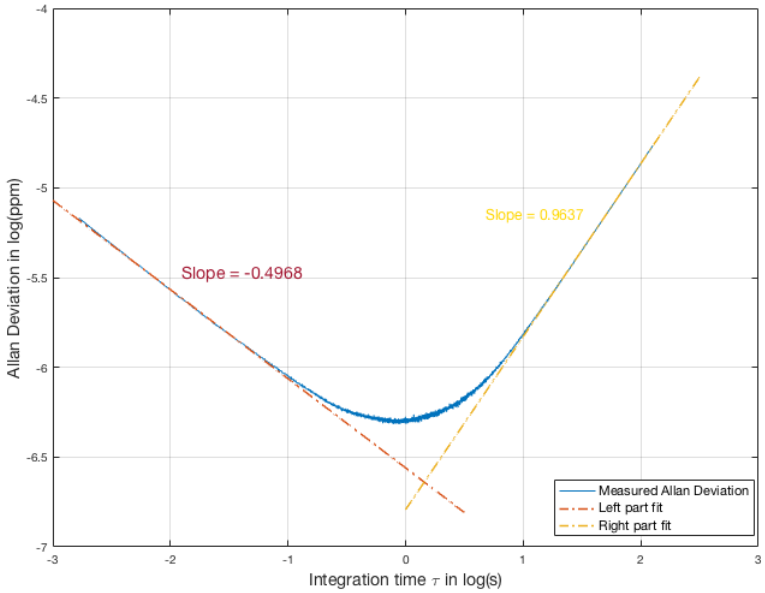

Figure 41: Plot of the Allan Devaiation versus integration time in logarithmic scale obtained for the SMR with a lower released volume together with the fitting line on both left and rigth parts

The slopes for both the structures are ~ -0.5 for the left part and ~ 1 for the right one confirming what expected from the theory: it is verified thus that the main noise contributions to the resonator sensitivity are due to the white noise - for low integration times - and frequency shift - for high integration times. Other important data to be taken from this measurements are the minimum AD value togehter with the relative integration time and, finally, the value of the Allan Deviation for integration time of 1 second. All these data of all the characterized strucutures are shown in tables 11, 12.

As shown in the tables, all the structures are characterized by the noise and the frequency shift noises as expected, even if the resonators whose realesed area is higher are closer to the ideal behaviour with respect to the others. Furthermore, the first exhibit AD below 10^{-6} for integration time of 1 second, while the others a little bit higher.

As a final check, it can be seen if there is any correlation between the Quality factor of the resonators and the corresponding magnitude

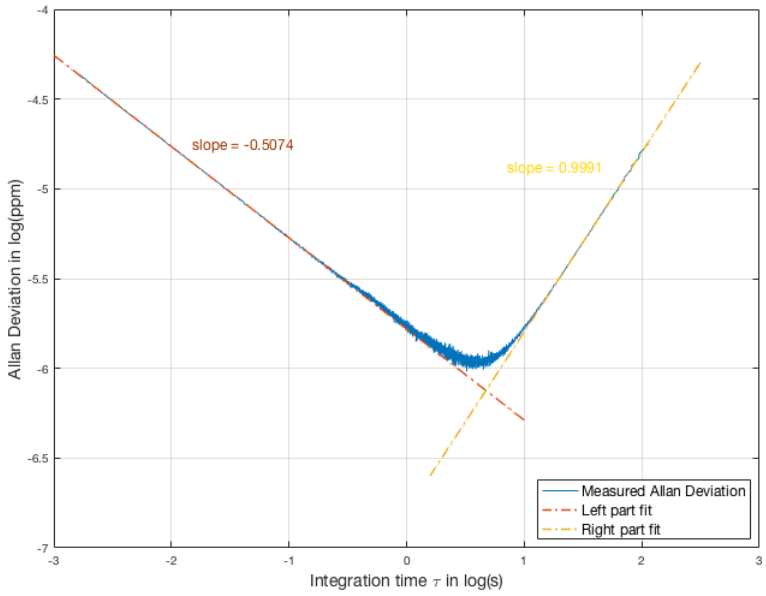

Figure 42: Plot of the Allan Deviation versus integration time in logarithmic scale obtained for the SMR with a higher released volume together with the fitting line on both left and rigth parts

Table 11: Data from the measurements performed on the low realeased volume resonators. In the table the minimum AD value with its correspondent integration time, the AD value for integration times of 1 second and the fitting slopes are reported.

SMR	1	2	3	4	5
min (ppm)	1	1	1	1	1
$\tau\|_{min}$ (s)	14.358	1.5965	6.2996	2.104	36.8586
$AD\|_{1sec}$ (ppm)	1	1	1	1	1
slope sx	-0.4953	-0.50046	-0.5173	-0.5080	-0.5015
slope dx	0.9637	0.9811	0.9373	0.9844	0.9458

Table 12: Data from the measurements performed on the high realeased volume resonators. In the table the minimum AD value with its correspondent integration time, the AD value for integration times of 1 second and the fitting slopes are reported.

SMR	1	2	3	4
$min\ (ppm))$	1	1	1	1
$\tau\|_{min}\ (s)$	0.2507	1.0662	0.8933	3.2469
$AD\|_{1sec}\ (ppm)$	1	1	1	1
slope sx	-0.5074	-0.5001	-0.4953	-0.5077
slope dx	0.9991	0.9427	0.9537	0.9794

of the white noise components. It is expected that for higher Q factor strucutures, the noise contribution is lower. To verify this, from the fitting equation (eq. 55) left part of the DA plot the q coefficient is taken and plottend for each of the structures. The resulting graph is shown in figure 43.

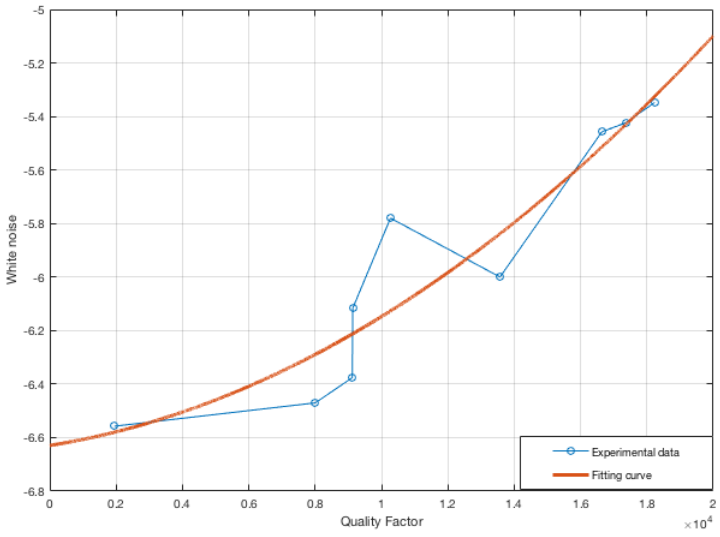

Figure 43: Plot of the magnitude of the white noise component (b coefficient in eq. 55) of the Allan Deviation in logarothmic scale versus the quality factor for all the tested structures

The expections are not confirmed by the previous plot, indeed the overall trend of the curve represented by the fitting curve is not decreasing, but grows up, meaning that the white noise component of the Allan Deviation is higher for structures characterized by higher Quality factor.

A final validation of the developed structure can be made by using the just proposed AD results together with the ones that come out

from the FEM simulations in order to translate them to actual limits of detections (LoD).
From the AD measurements comes out a minimum AD at 1 s pf 1 ppm. Presuming that AD becomes a factor 3 worse when the resonator is filled with liquid and considering a SNR value of at least 3, the signal should be of about $3 * 3 * 1$ $ppm \sim 10$ ppm. Looking now at the results from the FEM simulation, where the relative shift is $\sim$ 1000ppm and, for the expected AD of 3 ppm, the resonator would be characterized by a SNR of ~ 333, meaning that the sensor can ideally measure what it is set out to measure.
Based on these assumptions, it can be found, using equation 46 and considering the data assumed in table 13, that with the developed structure a $\Delta m \sim 150$ pg can be detected. Considering the immuno cell under test, with an average radius $\sim 7.1 \mu m$ and density $\sim 1000 kg/m^3$, the corresponding buoyant mass results of around $\sim 350 pg$ meaning that the developed resonator is able to detect it leading to a reasonable relative shift in the resonance frequency response.

Table 13: Material properties assumed for calculations.

Material property	SRN	Silicon	Water
Density (kg/m^3)	2800	2330	997.6
Volume (μm^3)	$\sim 3 \cdot 10^4$	~ 20	$\sim 2 \cdot 10^5$
Mass $(kg))$	$\sim 5 \cdot 10^{-11}$	$\sim 5 \cdot 10^{-14}$	$\sim 2 \cdot 10^{-10}$

7

CONCLUSIONS AND OUTLOOK

The aim of this work was to design, develop and characterize an integrated sensor for density, mass and viscosity spectrometry and also for IR absorption spectroscopy.
Starting from the already devoleped hollow MEMS resonator [16], the structure was optimized in order to obtain a sensor able to stop in the center of its channel the cell under test in order to analyze its response to a specific stimulus. In particular, all this work was built considering specific single immuno-cells.

The first optimization in the fabrication process regarded the back fluidic accesses. Performing a standard lithography step on the backside of the wafer followed by an isotropic etching through all the silicon wafer, four access holes have been fabricated for each structure. Two different dimensions have been designed, with a diameter of $50\mu m$ and $100\mu m$ respectively. In this step, the optimization of the anisotropic etching process was done in order to understand which was the exact number of cycles to be performed in order to reach the other side of the wafer, confirming at the end that for the bigger hole the number of cycles is higher and also the average etch rate is increased. That means that between the decreasing of the availability of the reactants due to the rise of the exposed area and the easier transport of reactive products due to the increaisng diameter, the last make a greater contribution leading to an overll increase of the average etch rate for higher diameter holes.
At this point, knowing the dimensions of the cell to be studied, the channel dimensions have been optimized in order to understand which was the isotropic etching time to be performed during the channel shaping. After having found that 25 minutes are as much as necessary to get a channel whose diameter is about $20\mu m$, another critical point was the shaping of the central point that needed to be also dimensioned with a diameter lower enough to trap the cell. In order to do this, the reticle was designed in order to build the channel joining two separated halves and by putting them at different distances. In such a way, performing the isotroping etching, the two halves meet in the center of the entire channel forming a hole whose dimension is strictly related to the distance between them. It has been found that the optimal distance was $14\mu m$ obtaining a central hole whos radius is $5\mu m$.

While the optimization of the fabrication was carried out, a finite element method based simulation was developed through the COMSOL Multiphysics software. The resonator was designed starting from the dimensions to be achieved for the final goal, in order to understand if such a thought structure could have sense from a resonating point of view . The device was simulated in its mechanical behaviour, by modeling its geometry in a simplified way, specifying the different materials - characterized by different mechanical properties - for each component of the model and by applying the right boundary conditions. The aim of this simulation was to undertand how the resonance frequency of the fundamental flexural mode of the structure changes during the moving of a cell immersed in a fluid inside the channel. Several parameters have been varied in order to be sure to consider different cases, in particular regarding the effective final entire channel mass and cell shape. All the implemented simulations have shown an acceptable normalized shift of the resonance frequency of about 1000 ppm that means, considering for example a noise signal < 100 ppm, to obtain a structure characterized by an acceptable SRN > 10.

The final part of the work was focused on the experiments necessary to characterized the resonance frequency behaviour and stability of the developed structures. In particular, exploiting an optical interferometric redout principle - LD vibrometer - first the exact resonance frequency and the quality factor of the structure have been measured, confirming the fact that the resonators were effectively released.
Furthermore, the structures resulted characterized by a quality factor that confirms the expectations from the literature, being in the range $10^3 - 10^4$.
Regarding the frequency stability characterization of a resonator MEMS, the AD was measured in order to understand which are the involved noise components limiting the sensitivity of the SCR. What comes from the results is that the white noise dominates the left side of the AD curve (low integration times) and the frequency shift the right one (high integration times), as expected from a theoretical point of view. A final important, even if unexpected consideration, was found in the correlation between the magnitude of the white noise component of a resonator and its quality factor. Indeed, against the expectations, it is found that structures with higher quality factor show higher noise.

Starting from these results, future work will go on to verify the sensor performances also in terms of mass sensitivity, filling the channel with liquids of different densities. Furthermore, IR spectroscopy measurements of the cell immobilized in the center constriction and also the measurement of the deformability and of the surface friction can be done.

The great property of the developed sensor is its versatility in terms of applications. Indeed even if in this work it is thought for sensing a kind of specific cells, it can be easily adapted for different biological entities - e.g. tumor cells - by simply knowing the average dimension of the cell. Indeed, the only requirement is to build a channel able to contain it and to trap the cell in its center, by simply varying the isotropic ething time during the channel shape defininition and the distance between the two channel halves.

Part V

APPENDIX

8

FABRICATION PROCESS FLOW

Step	Equipment	Procedure and Parameters
1 Preparation		
1.1	Wafers	4", 350µm, DSP Si wafers
2 SRN Deposition		
2.1	Furnace: LPCVD nitride	LPCVD deposition of ~ 320nm of nitride
3 Surface Channel Gaps		
3.1	Spin coater: SUSS Spinner-stepper6	Spin coating M35G, recipe 1402-DCH
3.2	DUV Stepper	Exposure, Reticle: PEEM-DUV 12-11-14
3.3	Developer: TMAH Stepper	Development, recipe 1003
3.4	AOE	Etch BARC, recipe barcetch, t = 1:30
3.5	AOE	SiN aniso etch, recipe SiO2_RES, t = 6:30
3.6	Plasma Asher 2	Strip resist, recipe 18, t = 30:00
4 Protective Layer Deposition		
4.1	PECVD 4	SiN PECVD dep, recipe LF SiN, t=16:00
5 Fluidic back inlets		
5.1	Spin Coater	Spin coating nLOF, recipe 2421
5.2	Aligner MA-6	Exposure, mask= '...DUV/2015/1-Back"
5.3	Developer:TMAH UV Lithography	Development, recipe
5.4	AOE	SiN aniso etch, recipe SiO2_RES, t = 2:30
5.5	DRIE Pegasus	Deep Si etch, recipe Process A
5.6	Plasma Asher 2	Strip resist, recipe 18, t = 30:00
5.7	BHF	Protective nitride stripe, t=65min
6 Channel Shaping		
6.1	DRIE Pegasus	Isot. Si etch, recipe mediumiso1, t=25:00
6.2	Plasma Asher 2	Strip resist, recipe 18, t = 30:00
7 Channel Closing		
7.1	RCA	RCA clean
7.2	Furnace: LPCVD nitride	LPCVD deposition of ~ 540nm of nitride
7.3	OM + Filmtek	Inspection , measure thckness
8 Resonator Release		
8.1	Spin Coater	Spin coating AZ 701 Mir, recipe 1411
8.2	Aligner MA-6	Exposure, mask= '...DUV/2014/3-Release"
8.3	Developer:TMAH UV Lithography	Development, recipe
8.4	AOE	SiN aniso etch, recipe SiO2_RES, t = 10:00
8.5	Plasma Asher 2	Strip resist, recipe 18, t = 30:00
8.6	DRIE Pegasus	Iso Si etch, recipe mediumiso1, t=10:00

BIBLIOGRAPHY

[1] J. Kim et al. "Hollow microtube resonators via silicon self-assembly towards sub-attogram mass sensing applications." In: *Nano Letters* (2016), pp. 1537–1545.

[2] A. Bryan et al. "Measurement of mass, density and volume during the cell cycle of yeast." In: *PNAS* (2010), pp. 999–1004.

[3] T. Burg and S. R. Manalis. "Suspended microchannel resonators for biomolecular detection." In: *Appl. Phys. Lett.* (2003), p. 2698.

[4] D. Ramos et al. "Detection of bacteria based on the thermomechanical noise of a nanomechanical resonator: origin of the response and detection limits." In: *Nanotechnology* 19.035503 (2008), p. 9.

[5] S. Byun et al. "Characterizing deformability and surface friction of cancer cells." In: *PNAS* (2013), pp. 7580–7585.

[6] G. Wu et al. "Bioassay of prostate-specific antigen (PSA) using microcantilevers." In: *Nat Biotechnol* (2001), pp. 856–860.

[7] Y. Weng et al. "Mass sensors with mechanical traps for weighing single cells in different fluids." In: *Lab Chip* (2011), p. 4174.

[8] A. De Pastina, M. D., and V. L.G. "Fabrication of suspended microchannel resonators with integrated piezoelectric transduction." In: *Microelectronic Engineering.* (2018), pp. 83–87.

[9] J. Kim et al. "Hollow microtube resonators via silicon self-assembly towards sub-attogram mass sensing applications." In: *Nano Letters* (2016), pp. 1537–1545.

[10] R. Calmo et al. ": Monolithic glass suspended microchannel resonators for enhanced mass sensing of liquids." In: *Sensors and Actuators B* (2018).

[11] T. Larsen et al. "Ultrasensitive string-based temperature sensors." In: *Appl. Phys. Lett.* (2011), p. 121901.

[12] T. Larsen et al. "Photothermal anlysis of individual nanoparticulate samples using micromechanical resonators." In: *ACS Nano* (2013), pp. 6188–93.

[13] S. Schimd et al. "Low-power photothermal probing of single plasmonic nanostructures with nanomechanical string resonators." In: *Nano Letters* (2014), pp. 1530–6984.

[14] S. Schmid, L. Villanueva, and M. Roukes. *Fundamentals of Nanomechanical Resonators*. Ed. by Springer. 2016. ISBN: 978-3-319-28689-1.

[15] K. L. Ekinci, Y. T. Yang, and M. L. Roukes. "Ultimate limits to inertial mass sensing based upon nanoelectromechanical systems." In: *J. Appl. Phys.* (2004), p. 2682.

[16] P. Larsen. *Hollow MEMS, An Integrated Sensor for Combined Density, Viscosity, Buoyant Mass and IR Absorption Spectrometry*. PhD Thesis.

[17] D. Scheible, A. Erbe, and R. Blick. "Dynamic control and modal analysis of coupled nano-mechanical resonators." In: *Appl. Phys. Lett.* (2003), p. 3333.

[18] C. prof. Ricciardi. *Nanomechanical Resonators notes from "Micro and Nanoscale Phenomena for Biomedicine"*. 2017-18.

[19] J. Sader, T. Burg, and S. Manalis. "Energy dissipation in microfluidic beam resonators: Dependence on mode number." In: *J. Appl. Phys.* (2010).

[20] J. Sader, T. Burg, and S. Manalis. "Energy dissipation in microfluidic beam resonators: Effext of Poisson's ratio." In: *Phys. Rev, E - Stat. Nonlinear, Soft Matter Phys.* (2011), pp. 1–15.

[21] K. L. Ekinci. "Electromechanical transducers at the nanoscale: actuation and sensing of motion in nanoelectromechanical systems (NEMS)." In: *Small* (2005), pp. 786–797.

[22] D. Karabacak, T. Kouh, and K. L. Ekinci. "Analysis of optical interferometric displacement detection in nanoelectromechanical systems." In: *Appl. Phys. Lett.* (2005), pp. 1–3.

[23] D. W. Allan and S. Leschiutta. "Atomic Frequency Standards." In: *Alta Freq.* (1974), pp. 221–230.

[24] L. Culter and C. Searle. "Some aspects of the theory and measurement of frequency fluctuations in frequency standards." In: *Proc. IEEE* (1966), pp. 136–154.

[25] Wikipedia. *Allan Variance*. https://en.wikipedia.org/wiki/Allan_variance.

[26] D. Logan. *A First Course in the Finite Element Method*. Ed. by Cl-Engineering. 5th ed. 2010. ISBN: 978-0495668251.

[27] W. B. J. Zimmerman. "Introduction to COMSOL Multiphysics." In: *Multiphysics Modeling with Finite Element Methods*. Citation Key: Zimmerman2006. World Scientific Publishing Company, 2006, pp. 1–26.

[28] Comsol. *Eigenfrequency Analysis*. https://www.comsol.it/multiphysics/eigenfrequency-analysis.

[29] D. I. Strikotov et al. "Is there a difference between T- and B-lynphocyte morphology?" In: *Journal of Biomedical Optics* 14.6 (2009).

[30] A. Polliack et al. “Identification of human B and T Lynphocytes by Scanning Electron Microscopy.” In: *Journal of Experimental Medicine* 138 (1973), pp. 607–624.

[31] prof. Cocuzza. *Epitaxy and CVD and PVD notes from "Physics of technological Process"*. 2017-18.

[32] prof. Cocuzza. *Lithography notes from "Physics of technological Process"*. 2017-18.

[33] B. Mozooni. “Optical Lithography.” In: *Techomat* (2015).

[34] D. Danchip. *Optical Lithography lecture notes*.

[35] prof. Cocuzza. *Dry etching notes from "Physics of technological Process"*. 2017-18.

[36] R. Egerton. *Physical principles of electron microscopy*. 2005.

[37] J. Burn. “Deep UV Lithography.” In: *Journal of Vacuum Science and Technology* (1998), p. 1975.

[38] P. Lutzmann et al. “Laser vibration sensing at Fraunhofer IOSB: review and applications.” In: *Oprical Engineering* 53 (2016), p. 3.

[39] Polytec. *Laser Doppler vibrometry*. https://www.polytec.com/int/vibrometry/technology.

[40] Z. Instruments. *HF2 User Manual - ziControl Edition*. Ed. by Z. I. AG. 2018.

[41] J. Lee et al. “Toward Attogram Mass Measurements in Solution with Suspended Nanochannel Resonators.” In: *Nano Lett.* 10.7 (2010), pp. 2537–2542.

[42] T. Burg et al. “Vacuum-Packaged Suspended Microchannel Resonant Mass Sensor for Biomolecular Detection.” In: *Journal of Microelectromechanical Systems* 15.6 (2006), pp. 1466–2476.

[43] J. Lee et al. “Suspended microchannel resonators with piezoresistive sensors.” In: *Lab Chip* 11.4 (2011), pp. 645–651.